A Fast and Efficient Method for Three-Dimensional Transient Electromagnetic Modeling Considering IP Effect

Qi Zhao, Huaifeng Sun, Shangbin Liu, Xushan Lu, Xixian Bai, Ziqiang Zheng

Abstract—Late-time negative responses in central-loop transient electromagnetic (TEM) data are often linked to the induced polarization (IP) effect. Early methods for modeling the IP effect in TEM data try to avoid calculating the fractional derivative arising from considering the Cole-Cole model by either using the Fourier transform to convert frequency-domain responses to the time domain or approximating the fractional derivative in the time domain directly. The frequency-to-time conversion method suffer from accuracy issues if the number of frequencies calculated is small. The time-domain approximation method also has accuracy issues because of simplified Cole-Cole models. The Caputo series can approximate fractional derivatives accurately if historic electromagnetic (EM) fields are saved. However, the storage of historic EM fields leads to a significant memory consumption. We introduce the sum-of-exponentials (SOE) method to discretize fractional derivatives, which does not need to store field values from previous times except for the first two time-steps. We discretize the resulting partial differential equations from the SOE discretization using a finite-difference time-domain (FDTD) approach. Additionally, we improve computational efficiency by employing the direct-splitting strategy to transform large sparse matrices into smaller diagonally dominant tridiagonal matrices. We validate the accuracy and efficiency of our algorithm by comparing it with the Caputo approximation method using a chargeable half-space model. Furthermore, we compare our results with existing literature data for a chargeable anomaly in a nonchargeable half space. Finally, we analyze the response characteristics of the IP effect using a block-in-half space model.

Index Terms—3D forward modeling, induced polarization (IP), Sum-of-exponentials (SOE), Finite different time method (FDTD), Backward Euler's direct-splitting (BEDS).

I. INTRODUCTION

THE transient electromagnetic (TEM) method is widely used in areas such as mineral exploration[1], hydrogeology [2], engineering investigation [3], [4]

Qi Zhao, Huaifeng Sun, Shangbin Liu, Ziqiang Zheng are with the Geotechnical and Structural Engineering Research Center, Shandong University, and the Laboratory of Earth Electromagnetic Exploration, Shandong University, Jinan, Shandong Province, 250000, China (e-mail: zhaoqi_326326@163.com, sunhuaifeng@email.sdu.edu.cn, liushangbin@email.edu.sdu.cn, 202385009035@sdu.edu.cn).
Xushan Lu is with the Department of Earth Sciences, Memorial University of Newfoundland, St. John's, 4200, Canada (xl0762@mun.ca).
Xixian Bai is with School of Mathematics and Statistics, Zhengzhou University, Zhengzhou 450001, China (xixianmath@zzu.edu.cn).

and environmental surveys [5]. Recently, increasing attention has been paid to the study of the induced polarization (IP) effect in TEM responses. Spies [6] pointed out that for coincident-loop devices, the IP effects can cause a sign reversal in late-time TEM data and this phenomenon was explained using the concept of complex conductivity. Recent studies further showed that the IP effect can seriously distort TEM field data and emphasized the importance of considering them in TEM data processing [7]. Li et al. [8] applied a Bayesian framework to decouple the IP effect in TEM data and recovered an accurate resistivity estimation from the data affected by IP effects. Grombacher et al. [9] carried out a survey over the McMurdo Dry Valleys and observed substantial IP effects in extensive regions within the survey area. that the IP effect in the TEM data caused conventional inversion workflows based on resistivity only struggle to fit observed data. Conventional inversion approaches treat the inductive portion of IP measurements as noise. Hence, its removal necessitates additional data processing steps [10]. In such cases, the presence of IP effects can lead to data becoming uninformative, significantly diminishing the utility of data for geological characterization purposes. Therefore, it is necessary to invert TEM data with inversion algorithms that can take chargeability into consideration when IP effects present. Consequently, it is important to develop accurate and efficient TEM forward modeling algorithms that consider the IP effect.

Many parametric models have been developed to describe the IP effect in TEM data and to explain the physical mechanisms behind it [11], such as the Dias model [12], the GEMIP model [13], and the Cole-Cole model [14]. The generally accepted mathematical model to describe the IP effect is the Cole-Cole model. The CCM was originally formulated for the complex dielectric constant [14]. For the complex resistivity model, Pelton et al. [15] proposed that it can be obtained directly from the original CCM equation by substituting the complex electrical resistivity for the complex dielectric constant:

$$\rho(\omega) = \rho_0 \left(1 - \eta \left(1 - \frac{1}{1 + (i\omega\tau)^c} \right) \right), \tag{1}$$

where ρ_0 represents the low-frequency electrical resistivity, η is the chargeability which reflects the polarizing capability of the medium [16], τ is the central relaxation time which controls the transition from high-frequency electrical

resistivity (inductive) to low-frequency electrical resistivity (DC) [7], c is the CCM exponent related to the broadness of central relaxation time distribution. The CCM becomes the Debye model if c is equal to 1 [17].

For the forward modeling considering CCM dispersion in the frequency domain, the constant resistivity should be replaced with the frequency-dependent complex resistivity. To model TEM data with the CCM dispersion, most of the early work first calculate the responses of polarizable bodies in the frequency domain and then transform them to the time domain [18]–[20]. However, when the electromagnetic field contains a broad band of frequency contents, responses of a large number of frequencies need to be calculated, and consequently many linear systems of equations should be solved to guarantee an accurate frequency-to-time transformation [21]. Thus, modeling the response of polarizable bodies in the time domain are likely more suitable for tackling large datasets [22]. However, the frequency-dependent complex electrical conductivity described by the CCM results in fractional-order time derivatives in the time domain, and their modeling directly in the time domain requires convolution calculation which is computationally challenging [23].

To circumvent these difficulties, some researchers presented certain approximation methods to simplify the CCM. For example, Commer [7] presented the auxiliary differential equation (ADE) method which effectively treats a CCM medium by approximating it with function expansions that are described by a differential equation with derivatives of integer order, that is, approximating the CCM by a series of weighted sum of different Debye relaxations. Marchant et al. [21] adopted the Padé approximation [24] to deal with the frequency-dependent dispersion of fractional function [25]. However, the accuracy of the resulting Padé approximation is determined by the order of the approximation used and the center point selected [21], [26], so the same parameter cannot match different waveforms. Cai et al. [27] developed a method to select the center point and orders for Padé series expansion adaptively during the time-stepping process, which improve the applicability of the algorithm. Ji et al. [28] used a frequency-domain rational approximation method and the linear programming technique to convert the fractional order system into an integer order one. However, the limitation is that the coefficients and relaxation times of approximation functions depend on CCM exponent.

In addition, some effective approximation methods were presented to directly solve Maxwell's equations with the CCM. Zaslavsky et al. [29], [30] developed a modeling technique based on the rational Krylov subspace projection approach to solve the time-domain Maxwell's equations in dispersive media. Zhang et al. [22] introduced the so-called Caputo method to approximate fractional derivatives, and they showed that their method has high accuracies expect for the sign reversal region. Liu et al.[31] used an unequal step length for the Caputo operator to consider the Maxwell's equations with heterogeneous medium. However, all electric and magnetic fields calculated in previous time steps need to be

stored in memory to calculate the field values for the next time step. When large meshes and a large number of modeling time steps are considered, the calculation speed can be low and the memory required to store all previous field values can be prohibitively expensive.

To sum up, we note that all previously mentioned methods that simplify the CCM by approximations to avoid solving the fractional derivatives have limitations, and directly solving the fractional derivatives is prohibitively expensive. Therefore, we need to find a method that does not require the storage of all prior fields at a given time step during the forward modeling process. Jiang et al. [32] presented an efficient algorithm for the evaluation of the Caputo fractional derivative. The algorithm is based on an efficient sum-of-exponentials (SOE) approximation for the power function with a uniform absolute error. Meanwhile, it consumes less memory because it does not require the explicit storage of all fields in the past [33]. Bai applied the SOE method to the electromagnetic field calculation with frequency-dependent relative permittivity functions and demonstrated its convergence [34], [35]. In this paper, we apply the SOE method to treat fractional derivative problems arising from the modeling of TEM data in dispersive media.

As a crucial tool, the finite-difference time-domain (FDTD) method have been widely developed to solve electromagnetic scattering issues, such as alternating-direction implicit FDTD [36]–[38], Crank-Nicolson FDTD [39]-[40], Crank-Nicolson direct-splitting FDTD [41], backward Euler direct-splitting FDTD (BEDS- FDTD) [42] and et al. In this paper, BEDS-FDTD method is used to discretize the partial differential equations (PDEs) obtained after the SOE approximation of Maxwell's equation with a CCM dispersion. Then the SOE-BEDS and Caputo-BEDS method are implemented to numerically simulate the fractional derivative. We validate SOE-BEDS algorithm by comparing the results with the solutions calculated for the Caputo-BEDS method and the results from the literature. Finally, we simulate and analyze the responses with various IP parameters to better understand how the IP effects affect TEM data.

II. METHODOLOGY

A. Governing Equation

Maxwell's equations in the time domain can be written as

$$\nabla \times \mathbf{e}(\mathbf{r},t) = -\mu \frac{\partial \mathbf{h}(\mathbf{r},t)}{\partial t} \qquad (2a)$$

$$\nabla \times \mathbf{h}(\mathbf{r},t) = \varepsilon \frac{\partial \mathbf{e}(\mathbf{r},t)}{\partial t} + \mathbf{j}(\mathbf{r},t) + \mathbf{j}_s(\mathbf{r},t), \qquad (2b)$$

where $\mathbf{e}$ and $\mathbf{h}$ represent the electric and magnetic fields, respectively, which are functions of time, t, and the position vector $\mathbf{r}(x, y, z)$; $\mathbf{j}_s$ is the source current density and $\mathbf{j}$ is the conductive current density; ε and μ denote permittivity and magnetic permeability, respectively. Then we describe the approach used for modeling chargeable materials in time-domain electromagnetic data. We start with materials

exhibiting Debye dispersion and then expand the approach to include CCM dispersions.

B. FDTD updating equations for Debye dispersive media

We review the relationship between $\mathbf{j}$ and $\mathbf{e}$ through Ohm's law:

$$\mathbf{j}(\mathbf{r},\omega) = \sigma(\omega)\mathbf{e}(\mathbf{r},\omega), \qquad (3)$$

where σ denotes the electrical conductivity. Conductivity in the Debye model can be expressed by [43]

$$\sigma(\omega) = \sigma_\infty \left(1 - \frac{\eta}{1+(1-\eta)(i\omega\tau)}\right). \qquad (4)$$

In this equation, σ_∞ is the high-frequency electrical conductivity. Substituting equation 4 into equation 3, we obtain

$$\mathbf{j}(\mathbf{r},t) + \tau(1-\eta)(i\omega)\mathbf{j}(\mathbf{r},t) = \sigma_\infty(1-\eta)\mathbf{e}(\mathbf{r},t) \\ + \sigma_\infty\tau(1-\eta)(i\omega)\mathbf{e}(\mathbf{r},t). \qquad (5)$$

Applying the Fourier transform, $\mathcal{F}(\partial f(t)/\partial t) = i\omega F(\omega)$, gives

$$\mathbf{j}(\mathbf{r},t) + \tau(1-\eta)\frac{\partial \mathbf{j}(\mathbf{r},t)}{\partial t} = \sigma_\infty(1-\eta)\mathbf{e}(\mathbf{r},t) + \sigma_\infty\tau(1-\eta)\frac{\partial \mathbf{e}(\mathbf{r},t)}{\partial t}. \qquad (6)$$

Substituting equation 6 into Ampere's law (equation 2b) yields

$$\nabla \times \mathbf{h}(\mathbf{r},t) = \left[\varepsilon + \sigma_\infty\tau(1-\eta)\right]\frac{\partial \mathbf{e}(\mathbf{r},t)}{\partial t} + \sigma_\infty(1-\eta)\mathbf{e}(\mathbf{r},t) \\ - \tau(1-\eta)\frac{\partial \mathbf{j}(\mathbf{r},t)}{\partial t} + \mathbf{j}_s(\mathbf{r},t). \qquad (7)$$

We use the central difference (CD) scheme to discretize the above equation in space. The staggered Yee grid [44] is used to discretize the computational domain. The electric field is defined at the center of mesh edges while the magnetic field is defined at the center of mesh faces (Figure 1).
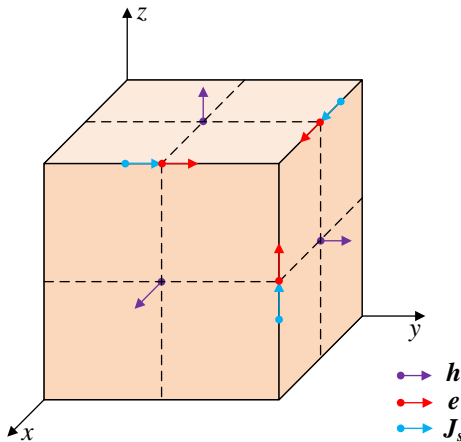

Fig. 1. A single cell from the Yee grid used for the discretization of the computational domain. Electric fields and source current densities are assigned on cell edges. Magnetic fields are assigned on cell faces. Material properties are assigned at cell centers.

The semi-discretization of equations 2a and 7 can be written as

$$D_{\zeta+1}\mathbf{e}_{\zeta-1}(t) - D_{\zeta-1}\mathbf{e}_{\zeta+1}(t) = -\mu\frac{\partial \mathbf{h}_\zeta(t)}{\partial t} \qquad (8a)$$

$$D_{\zeta+1}\mathbf{h}_{\zeta-1}(t) - D_{\zeta-1}\mathbf{h}_{\zeta+1}(t) = \left[\varepsilon + \sigma_\infty\tau(1-\eta)\right]\frac{\partial \mathbf{e}_\zeta(t)}{\partial t} \\ + \sigma_\infty(1-\eta)\mathbf{e}_\zeta(t) - \tau(1-\eta)\frac{\partial \mathbf{j}_\zeta(t)}{\partial t} + \mathbf{j}_{s_\zeta}(t), \qquad (8b)$$

where D_ζ is defined as the first-order central difference operators [41], and ζ denotes the coordinates in the x-, y-, and z-directions. The unconditionally stable, first-order backward Euler (BE) method is adopted to discretize the time derivatives in equation 8:

$$D_{\zeta+1}\mathbf{e}_{\zeta-1}^{n+1} - D_{\zeta-1}\mathbf{e}_{\zeta+1}^{n+1} = -\mu\frac{\mathbf{h}_\zeta^{n+1} - \mathbf{h}_\zeta^n}{\Delta t_n} \qquad (9a)$$

$$D_{\zeta+1}\mathbf{h}_{\zeta-1}^{n+1} - D_{\zeta-1}\mathbf{h}_{\zeta+1}^{n+1} = \left[\varepsilon + \sigma_\infty\tau(1-\eta)\right]\frac{\mathbf{e}_\zeta^{n+1} - \mathbf{e}_\zeta^n}{\Delta t_n} \\ + \sigma_\infty(1-\eta)\mathbf{e}_\zeta^{n+1} - \tau(1-\eta)\frac{\mathbf{j}_\zeta^{n+1} - \mathbf{j}_\zeta^n}{\Delta t_n} + \mathbf{j}_{s_\zeta}^{n+1}, \qquad (9b)$$

where the superscripts n and $n+1$ denote the field values at the past and current times, t_n and t_{n+1}, respectively. The time step size can be calculated by $\Delta t_n = t_{n+1} - t_n$. Similarly, applying the BE method to equation 6, we can obtain the updating equation for current density, with respects to $\mathbf{e}(\mathbf{r})$:

$$\mathbf{j}^{n+1}(\mathbf{r}) = \sigma_\infty\frac{(\Delta t_n + \tau)(1-\eta)}{\Delta t_n + \tau(1-\eta)}\mathbf{e}^{n+1}(\mathbf{r}) \\ + \frac{\tau(1-\eta)}{\Delta t_n + \tau(1-\eta)}\mathbf{j}^n(\mathbf{r}) - \frac{\sigma_\infty\tau(1-\eta)}{\Delta t_n + \tau(1-\eta)}\mathbf{e}^n(\mathbf{r}). \qquad (10)$$

Then, considering equations 10 and 9, we obtain the discretization for the magnetic- and electric-field components at time t_{n+1}:

$$\begin{cases} e_\zeta^{n+1} + a_1 D_{\zeta-1}h_{\zeta+1}^{n+1} - a_1 D_{\zeta+1}h_{\zeta-1}^{n+1} = a_0 e_\zeta^n - a_2 j_\zeta^n + j_{s_\zeta}^{n+1}, \\ -d_0 D_{\zeta-1}e_{\zeta+1}^{n+1} + d_0 D_{\zeta+1}e_{\zeta-1}^{n+1} + h_\zeta^{n+1} = h_\zeta^n, \end{cases} \qquad (11)$$

where

$$a_0 = \left(\varepsilon + \Delta t_n\frac{\sigma_\infty\tau(1-\eta)}{\Delta t_n + \tau(1-\eta)}\right) / \left(\varepsilon + \Delta t_n\sigma_\infty - \frac{\Delta t_n^2\sigma_\infty\eta}{\Delta t_n + \tau(1-\eta)}\right),$$

$$a_1 = \Delta t_n / \left(\varepsilon + \Delta t_n\sigma_\infty - \frac{\Delta t_n^2\sigma_\infty\eta}{\Delta t_n + \tau(1-\eta)}\right), d_0 = \Delta t_n / \mu,$$

$$a_2 = \Delta t_n\frac{\tau(1-\eta)}{\Delta t_n + \tau(1-\eta)} / \left(\varepsilon + \Delta t_n\sigma_\infty - \frac{\Delta t_n^2\sigma_\infty\eta}{\Delta t_n + \tau(1-\eta)}\right).$$

C. FDTD updating equations for CCM dispersive media

It is widely accepted that for most chargeable materials, the value of CCM exponent is a positive real number smaller than

1 [47], [48]. For materials that exhibit a CCM dispersion, equation 1 can be rewritten as [43]

$$\sigma(\omega) = \sigma_0 \left(1 + \eta \left(\frac{(i\omega\tau)^c}{1 + (i\omega\tau)^c (1-\eta)} \right) \right), \quad (12)$$

where σ_0 is the low-frequency electrical conductivity that can be expressed by σ_∞, namely, $\sigma_0 = \sigma_\infty (1-\eta)$ [43]. Substituting equation 12 into equation 3 gives the following:

$$\mathbf{j}(\mathbf{r},t) + (1-\eta)\tau^c \frac{\partial^c \mathbf{j}(\mathbf{r},t)}{\partial t^c} = \sigma_0 \mathbf{e}(\mathbf{r},t) + \sigma_0 \tau^c \frac{\partial^c \mathbf{e}(\mathbf{r},t)}{\partial t^c}. (13)$$

There are fractional derivatives on both sides of equation 13 because c is no longer an integer. The Caputo fractional derivative of order c is defined as:

$$\frac{\partial^c f(t)}{\partial t^c} = \frac{1}{\Gamma(1-c)} \int_0^t \frac{f'(m)}{(t-m)^c} dm, \quad 0 < c < 1, \quad (14)$$

where Γ is the Gamma function. Dividing the time interval from 0 to t into n steps, we have $0 = t_0 < \ldots < t_p < \ldots < t_n = t$, and $\Delta t_p = t_{p+1} - t_p$, where $p = 0, 1, \ldots, n-1$. Considering the Caputo fractional derivative within $[t_{p-1}, t_p]$, We discretize equation 14 using the $L1$-approximation [49]. The derivation process is identical to Appendix A1. Then the following equation is obtained:

$$\frac{\partial^c f(t_n)}{\partial t^c} = \frac{1}{\Gamma(1-c)} \int_0^{t_n} \frac{f'(m)}{(t-m)^c} dm$$

$$= \frac{1}{\Gamma(2-c)} \left[\frac{b_{n-1}^n}{\Delta t_{n-1}} f(t_n) - \sum_{p=1}^{n-1} \left(\frac{b_p^n}{\Delta t_p} - \frac{b_{p-1}^n}{\Delta t_{p-1}} \right) f(t_p) \right], (n \geq 2)$$

(15)

In the above equation, we define $b_p^n = \left[(t_n - t_p)^{1-c} - (t_n - t_{p+1})^{1-c} \right]$.

When $n=0$ and $n=1$, we have

$$\frac{\partial^c f(t_n)}{\partial t^c} = \frac{1}{\Gamma(2-c)} \left[\frac{b_0^n}{\Delta t_0} (f(t_1) - f(t_0)) \right], (n=1)$$

$$\frac{\partial^c f(t_n)}{\partial t^c} = 0. (n=0) \quad (16)$$

The fractional time derivatives of $\mathbf{j}^n(\mathbf{r})$ and $\mathbf{e}^n(\mathbf{r})$ at time t_n can be expressed as:

$$\begin{cases} \frac{\partial^c \mathbf{j}^n(\mathbf{r})}{\partial t^c} = \frac{1}{\Gamma(2-c)} \left[\frac{1}{(\Delta t_{n-1})^c} \mathbf{j}^n(\mathbf{r}) - \sum_{p=1}^{n-1} \left(\frac{b_p^n}{\Delta t_p} - \frac{b_{p-1}^n}{\Delta t_{p-1}} \right) \mathbf{j}^p(\mathbf{r}) \right], \\ \frac{\partial^c \mathbf{e}^n(\mathbf{r})}{\partial t^c} = \frac{1}{\Gamma(2-c)} \left[\frac{1}{(\Delta t_{n-1})^c} \mathbf{e}^n(\mathbf{r}) - \sum_{p=1}^{n-1} \left(\frac{b_p^n}{\Delta t_p} - \frac{b_{p-1}^n}{\Delta t_{p-1}} \right) \mathbf{e}^p(\mathbf{r}) \right]. \end{cases} (17)$$

Substituting equations 17 into equation 13, we have updating equation of current density with CCM dispersion at time t_{n+1}:

$$\mathbf{j}^{n+1}(\mathbf{r}) = \frac{K_2^n}{K_1^n} \mathbf{e}^{n+1}(\mathbf{r}) + \frac{K_3}{K_1^n} \mathbf{M}_j^n(\mathbf{r}) - \frac{K_4}{K_1^n} \mathbf{M}_e^n(\mathbf{r}), \quad (18)$$

where

$$\begin{cases} K_1^n = 1 + \frac{(1-\eta)\tau^c}{(\Delta t_n)^c \Gamma(2-c)}, K_2^n = \sigma_0 + \frac{\sigma_0 \tau^c}{(\Delta t_n)^c \Gamma(2-c)}, \\ K_3 = \frac{(1-\eta)\tau^c}{\Gamma(2-c)}, \mathbf{M}_j^n(\mathbf{r}) = \sum_{p=1}^n \left(\frac{b_p^{n+1}}{\Delta t_p} - \frac{b_{p-1}^{n+1}}{\Delta t_{p-1}} \right) \mathbf{j}^p(\mathbf{r}), \\ K_4 = \frac{\sigma_0 \tau^c}{\Gamma(2-c)}, \mathbf{M}_e^n(\mathbf{r}) = \sum_{p=1}^n \left(\frac{b_p^{n+1}}{\Delta t_p} - \frac{b_{p-1}^{n+1}}{\Delta t_{p-1}} \right) \mathbf{e}^p(\mathbf{r}). \end{cases} (19)$$

Note, $\mathbf{M}_j^n$ and $\mathbf{M}_e^n$ need to be recalculated for each time step, and the number of terms in the summation increases as n increases. Considering equations 18, full discretization of Maxwell's equations considering the CCM dispersion are

$$\begin{cases} e_\zeta^{n+1} + a_1' D_{\zeta-1} h_{\zeta+1}^{n+1} - a_1' D_{\zeta+1} h_{\zeta-1}^{n+1} = a_0' e_\zeta^n - a_2' M_{j_\zeta}^n + a_3' M_{e_\zeta}^n + j_{s_\zeta}^{n+1}, \\ -d_0 D_{\zeta-1} e_{\zeta+1}^{n+1} + d_0 D_{\zeta+1} e_{\zeta-1}^{n+1} + h_\zeta^{n+1} = h_\zeta^n, \end{cases}$$

(20)

where

$$\begin{cases} a_0' = \varepsilon / \left(\varepsilon + \Delta t_n \frac{K_2^n}{K_1^n} \right), a_2' = \Delta t_n \frac{K_3}{K_1^n} / \left(\varepsilon + \Delta t_n \frac{K_2^n}{K_1^n} \right), \\ a_1' = \Delta t_n / \left(\varepsilon + \Delta t_n \frac{K_2^n}{K_1^n} \right), a_3' = \Delta t_n \frac{K_4}{K_1^n} / \left(\varepsilon + \Delta t_n \frac{K_2^n}{K_1^n} \right). \end{cases}$$

D. Approximations for Caputo derivative

In the above section where we discretized Maxwell's equations considering the CCM dispersion model with the Caputo-BEDS Method, we have to recalculate $\mathbf{M}_j^n$ and $\mathbf{M}_e^n$ from equation 19 for each time step [32]. The computational complexity of this method is $\mathcal{O}(N_n^2 N_s)$, where N_n and N_s are the number of time steps and mesh grids used to discretize the model, respectively. We need to store all previous fields, so it requires on average $\mathcal{O}(N_n)$ memory and the total computational cost is $\mathcal{O}(N_n^2)$. And it is evident that both memory usage and calculation time increase with the number of time steps.

To improve computing speed and reduce memory consumption, we use SOE algorithm to solving equation 15. This algorithm is based on an efficient approximation for the kernel t^{-1-c} on the interval [0, 1].

Equation 15 can be rewritten as the sum of a local term and a historical term [32]:

$$\frac{\partial^c f(t_n)}{\partial t^c} = \frac{1}{\Gamma(1-c)} \int_0^{t_n} \frac{f'(m)}{(t-m)^c} dm$$

$$= \frac{1}{\Gamma(1-c)} \int_{t_{n-1}}^{t_n} \frac{f'(m) dm}{(t_n-m)^c} + \frac{1}{\Gamma(1-c)} \int_0^{t_{n-1}} \frac{f'(m) dm}{(t_n-m)^c} \quad (21)$$

$$= C_l(t_n) + C_h(t_n),$$

where the local term can be calculated using the $L1$-approximation [49]:

$$C_l(t_n) = \frac{f(t_n) - f(t_{n-1})}{\Delta t_{n-1} \Gamma(1-c)} \int_{t_{n-1}}^{t_n} \frac{dm}{(t_n-m)^c} = \frac{f(t_n) - f(t_{n-1})}{\Delta t_{n-1}^c \Gamma(2-c)}. (22)$$

For the historical term, integration by parts is adopted to

eliminate $f'(m)$:

$$
\begin{aligned}
C_h(t_n) &= \frac{1}{\Gamma(1-c)}\int_0^{t_{n-1}}\frac{f'(m)\,dm}{(t_n-m)^c} \\
&= \frac{1}{\Gamma(1-c)}\left[\frac{f(t_{n-1})}{\Delta t_{n-1}^c}-\frac{f(t_0)}{t_n^c}-c\int_0^{t_{n-1}}\frac{f(m)\,dm}{(t_n-m)^{1+c}}\right].
\end{aligned}
\tag{23}
$$

The kernel $(t_n-m)^{-(1+c)}$ $(0<c<1)$ from equation 23 can be approximated via the SOE method on the interval $[\vartheta, t]$, where $\vartheta=\min \Delta t_n$ and δ represents an uniform absolute error [32]. We can obtain

$$
\left|\frac{1}{(t_n-m)^{1+c}}-\sum_{v=1}^{N_{\exp}}\xi_v e^{-s_v(t_n-m)}\right|\le \delta, \qquad m\in[\vartheta,t].
\tag{24}
$$

The s_v and ξ_v (v=1, …, $N_{\exp}$) are the nodes and weights for n-point Gauss-Legendre quadrature [32], however, the number of nodes and the value of weights depends on the complier but the approximate accuracy is not affected. The number of exponentials needed is of the order $N_{\exp} = \mathcal{O}\left(\log\frac{1}{\delta}(\log\log\frac{1}{\delta}+\log\frac{t}{\vartheta})+\log\frac{1}{\vartheta}(\log\log\frac{1}{\delta}+\log\frac{1}{\vartheta})\right)$.

Considering equation 24, equation 23 can be rewritten as

$$
C_h(t_n)\approx\frac{1}{\Gamma(1-c)}\left[\begin{array}{l}\dfrac{f(t_{n-1})}{\Delta t_{n-1}^c}-\dfrac{f(t_0)}{t_n^c}\\[2mm]-c\displaystyle\sum_{v=1}^{N_{\exp}}\xi_v\int_0^{t_{n-1}}\left(e^{-s_v(t_n-m)}f(m)+\delta\right)dm\end{array}\right].
\tag{25}
$$

Ignoring δ, which is a positive real number greater than 0 and an extremely small value, and setting the initial field value to 0, then equation 21 can be rearranged as following:

$$
\begin{aligned}
\frac{\partial^c f(t_n)}{\partial t^c}&\approx\frac{f(t_n)-f(t_{n-1})}{\Delta t_{n-1}^c\Gamma(2-c)}\\
&+\frac{1}{\Gamma(1-c)}\left[\frac{f(t_{n-1})}{\Delta t_{n-1}^c}-c\sum_{v=1}^{N_{\exp}}\xi_v\int_0^{t_{n-1}}\left(e^{-s_v(t_n-m)}f(m)\right)dm\right].
\end{aligned}
\tag{26}
$$

Substituting equation 26 into equation 13, we can get the updating equation of current density with CCM dispersion at time Δt_{n+1}:

$$
\begin{aligned}
&\left(1+\frac{(1-\eta)\tau^c}{\Delta t_n^c\Gamma(2-c)}\right)\mathbf{j}^{n+1}\approx\left(\frac{\sigma_0+}{\frac{\sigma_0\tau^c}{\Delta t_n^c\Gamma(2-c)}}\right)\mathbf{e}^{n+1}+\left(\frac{\frac{(1-\eta)\tau^c}{\Delta t_n^c\Gamma(2-c)}}{-\frac{(1-\eta)\tau^c}{\Delta t_n^c\Gamma(1-c)}}\right)\mathbf{j}^n\\
&-\left(\frac{\frac{\sigma_0\tau^c}{\Delta t_n^c\Gamma(2-c)}}{-\frac{\sigma_0\tau^c}{\Delta t_n^c\Gamma(1-c)}}\right)\mathbf{e}^n+\frac{c(1-\eta)\tau^c}{\Gamma(1-c)}\sum_{i=1}^{N_{\exp}}\omega_i\int_0^{t_n}\left(e^{-s_i(t_{n+1}-m)}\mathbf{j}^m\right)dm\\
&-\frac{c\sigma_0\tau^c}{\Gamma(1-c)}\sum_{i=1}^{N_{\exp}}\omega_i\int_0^{t_n}\left(e^{-s_i(t_{n+1}-m)}\mathbf{e}^m\right)dm.
\end{aligned}
\tag{27}
$$

Rearranging equation 27, we have

$$
\begin{aligned}
\mathbf{j}^{n+1}(\mathbf{r})&\approx\frac{K_2^n}{K_1^n}\mathbf{e}^{n+1}(\mathbf{r})+\frac{\bar{K}_3^n}{K_1^n}\mathbf{j}^n(\mathbf{r})-\frac{\bar{K}_4^n}{K_1^n}\mathbf{e}^n(\mathbf{r})\\
&+\frac{K_5^n}{K_1^n}\mathbf{M}_j^n(\mathbf{r})-\frac{K_6^n}{K_1^n}\mathbf{M}_e^n(\mathbf{r}),
\end{aligned}
\tag{28}
$$

where

$$
\begin{cases}
\bar{K}_3^n=\dfrac{(1-\eta)\tau^c}{\Delta t_n^c\Gamma(2-c)}-\dfrac{(1-\eta)\tau^c}{\Delta t_n^c\Gamma(1-c)},K_5=\dfrac{c(1-\eta)\tau^c}{\Gamma(1-c)}\\[3mm]
\bar{K}_4^n=\dfrac{\sigma_0\tau^c}{\Delta t_n^c\Gamma(2-c)}-\dfrac{\sigma_0\tau^c}{\Delta t_n^c\Gamma(1-c)},K_6=\dfrac{c\sigma_0\tau^c}{\Gamma(1-c)},
\end{cases}
\tag{29a}
$$

$$
\begin{cases}
\mathbf{M}_j^n(\mathbf{r})=\displaystyle\sum_{v=1}^{N_{\exp}}\xi_v\int_0^{t_n}\left(e^{-s_v(t_{n+1}-m)}\mathbf{j}^m\right)dm,\\[3mm]
\mathbf{M}_e^n(\mathbf{r})=\displaystyle\sum_{v=1}^{N_{\exp}}\xi_v\int_0^{t_n}\left(e^{-s_v(t_{n+1}-m)}\mathbf{e}^m\right)dm.
\end{cases}
\tag{29b}
$$

Now we should tackle the complex summation terms in equation 29b and define

$$
U_{h,v}(t_n)=\int_0^{t_n}\left(e^{-s_v(t_{n+1}-m)}f(m)\right)dm,
\tag{30}
$$

where h represents the e or j, corresponding to $\mathbf{e}(\mathbf{r}, m)$ and $\mathbf{j}(\mathbf{r}, m)$ respectively. Equation 30 can be easily expressed as the recurrence relation:

$$
U_{h,v}(t_n)=e^{-s_v\Delta t_n}U_{h,v}(t_{n-1})+\int_{t_{n-1}}^{t_n}e^{-s_v(t_{n+1}-m)}f(m)\,dm.
\tag{31}
$$

At each time step, the $\mathcal{O}(1)$ calculation only needs to consider $U_{h,v}(t_n)$ which can be calculated from $U_{h,v}(t_{n-1})$ that is known from the previous time step. Whole calculation process need $\mathcal{O}(N_{exp})$ memory compared with the Caputo approximation method. As a result, the total calculation is reduced from $\mathcal{O}(N_n^2)$ to $\mathcal{O}(N_tN_{exp})$. Based on numerical experiments, it is found that N_{exp} does not have to be large even when the TEM modeling has a long period of time after the source current is switched off. For the second term on the right-hand side of equation 31, we can calculate by linear interpolation and integration by parts method. The derivation process is given in detail in Appendix A2 [32]. Eventually, we can write the second term of the right-hand side of equation 31 as

$$
\begin{aligned}
&\int_{t_{n-1}}^{t_n}e^{-s_v(t_{n+1}-m)}f(m)\,dm\\
&=\frac{e^{-s_v\Delta t_n}}{s_v^2\Delta t_{n-1}}\left[\begin{array}{l}\left(e^{-s_v\Delta t_{n-1}}-1+s_i\Delta t_{n-1}\right)f(t_n)\\[2mm]+\left(1-e^{-s_v\Delta t_{n-1}}-s_v e^{-s_v\Delta t_{n-1}}\Delta t_{n-1}\right)f(t_{n-1})\end{array}\right].
\end{aligned}
\tag{32}
$$

Considering equations 28-32, the full discretization of equations 2 are written as follows:

$$
\begin{cases}
e_\zeta^{n+1}+a_1'D_{\zeta-1}h_{\zeta+1}^{n+1}-a_1'D_{\zeta+1}h_{\zeta-1}^{n+1}=a_0''e_\zeta^n-a_2''j_\zeta^n-a_3''M_{j\zeta}^n+a_4''M_{e\zeta}^n+j_{s\zeta}^{n+1},\\
-d_0D_{\zeta-1}e_{\zeta+1}^{n+1}+d_0D_{\zeta+1}e_{\zeta-1}^{n+1}+h_\zeta^{n+1}=h_\zeta^n,
\end{cases}
\tag{33}
$$

where:

$$\begin{cases} a_0'' = \left(\varepsilon + \Delta t_n \frac{\bar{K}_4^n}{K_1^n}\right)\Big/\left(\varepsilon + \Delta t_n \frac{K_2^n}{K_1^n}\right), a_2'' = \Delta t_n \frac{\bar{K}_3^n}{K_1^n}\Big/\left(\varepsilon + \Delta t_n \frac{K_2^n}{K_1^n}\right), \\ a_3'' = \Delta t_n \frac{K_5^n}{K_1^n}\Big/\left(\varepsilon + \Delta t_n \frac{K_2^n}{K_1^n}\right), a_4'' = \Delta t_n \frac{K_6^n}{K_1^n}\Big/\left(\varepsilon + \Delta t_n \frac{K_2^n}{K_1^n}\right). \end{cases}$$

E. Direct-Splitting Method

Note that solving the sparse linear system of equations (equation 11, equation 20, and equation 33) directly with either direct or iterative solvers is a computationally expensive process [45]. In this paper, the DS approach is used to divide the sparse matrix into smaller tridiagonal matrices so that the linear system of equation can be solved more efficiently [41], [42].

The matrix form of equation 11 can be written as

$$\left(\mathbf{I}_6 - \mathbf{A} - \mathbf{B}\right)\mathbf{W}^{n+1} = \mathbf{C}\mathbf{W}^n + \mathbf{X}_1\mathbf{J}^n + \mathbf{J}_s^{n+1}, \qquad (34)$$

where $\mathbf{I}_6$ is an identity matrix of 6×6 and $\mathbf{W} = [e_x \; e_y \; e_z \; h_x \; h_y \; h_z]^T$. $\mathbf{J}_s$ is the source vector, and other matrixes are defined as follows:

$$\begin{cases} \mathbf{A} = \begin{bmatrix} 0 & -a_1\mathbf{R} \\ -d_0\mathbf{R}^T & 0 \end{bmatrix}, \mathbf{B} = \begin{bmatrix} 0 & a_1\mathbf{R}^T \\ d_0\mathbf{R} & 0 \end{bmatrix}, \\ \mathbf{C} = \begin{bmatrix} a_0\mathbf{I}_3 & 0 \\ 0 & \mathbf{I}_3 \end{bmatrix}, \mathbf{X}_1 = \begin{bmatrix} -a_2 & 0 \\ 0 & 0 \end{bmatrix}. \end{cases} \qquad (35)$$

The matrix R in A and B is defined as:

$$\mathbf{R} = \begin{bmatrix} 0 & D_z & 0 \\ 0 & 0 & D_x \\ D_y & 0 & 0 \end{bmatrix}$$

Adding a higher-order error term $\mathbf{AB}(\mathbf{W}^{n+1}-\mathbf{W}^n)$ into both sides of equation 34, we get

$$\left(\mathbf{I}_6 - \mathbf{A}\right)\left(\mathbf{I}_6 - \mathbf{B}\right)\mathbf{W}^{n+1} = \left(\mathbf{C} + \mathbf{AB}\right)\mathbf{W}^n + \mathbf{X}_1\mathbf{J}^n + \mathbf{J}_s^{n+1}. \quad (36)$$

Factoring the left-hand side of equation 36 yields

$$\begin{cases} \left(\mathbf{I}_6 - \mathbf{A}\right)\mathbf{W}^* = \left(\mathbf{C} + \mathbf{B}\right)\mathbf{W}^n + \mathbf{X}_1\mathbf{J}^n + \mathbf{J}_s^{n+1}, \\ \left(\mathbf{I}_6 - \mathbf{B}\right)\mathbf{W}^{n+1} = \mathbf{W}^* - \mathbf{B}\mathbf{W}^n, \end{cases} \qquad (37)$$

where $\mathbf{W}^* = [e_x^* \; e_y^* \; e_z^* \; h_x^* \; h_y^* \; h_z^*]^T$ are auxiliary fields and don't have physical meanings. Substituting equation 35 into equation 37 and performing the expansion operation give:

$$\begin{cases} \left(\mathbf{I}_3 - a_1 d_0 \mathbf{R}\mathbf{R}^T\right)\mathbf{e}^* = \left(a_0\mathbf{I}_3 - a_1 d_0 \mathbf{R}\mathbf{R}\right)\mathbf{e}^n \\ \qquad\qquad + \left(a_1\mathbf{R}^T - a_1\mathbf{R}\right)\mathbf{h}^n - a_2\mathbf{J}^n + \mathbf{J}_s^{n+1}, \\ \left(\mathbf{I}_3 - d_0 a_1 \mathbf{R}^T\mathbf{R}\right)\mathbf{e}^{n+1} = \mathbf{e}^* - d_0 a_1 \mathbf{R}^T\mathbf{R}^T\mathbf{e}^*, \\ \mathbf{h}^{n+1} = \mathbf{h}^n - d_0 \mathbf{R}^T\mathbf{e}^* + d_0 \mathbf{R}\mathbf{e}^{n+1}. \end{cases} \qquad (38)$$

Substituting $\mathbf{R}$ into the above equation and considering the Dirichlet boundary condition, we can get the final full discretization of Maxwell's equations considering the Debye

dispersion (referred to as Debye-BEDS):

$$\left(1 - a_1 d_0 D_{2(\varsigma-1)}\right)e_\varsigma^* = a_0 e_\varsigma^n - a_1 d_0 D_\varsigma D_{\varsigma-1} e_{\varsigma-1}^n \\ + a_1 D_{\varsigma+1} h_{\varsigma-1}^n - a_1 D_{\varsigma-1} h_{\varsigma+1}^n - a_2 j_\varsigma^n + j_{s_\varsigma}^{n+1}, \qquad (39a)$$

$$\left(1 - a_1 d_0 D_{2(\varsigma+1)}\right)e_\varsigma^{n+1} = e_\varsigma^* - a_1 d_0 D_\varsigma D_{\varsigma+1} e_{\varsigma+1}^*, \qquad (39b)$$

$$h_\varsigma^{n+1} = h_\varsigma^n - d_0 D_{\varsigma+1} e_{\varsigma-1}^* + d_0 D_{\varsigma-1} e_{\varsigma+1}^{n+1}, \qquad (39c)$$

where $D_{2\varsigma}$ in these equations represents the second order central difference operator. It should be noted that equation 39a and 39b can be solved by the Thomas algorithm [46] because their coefficient matrices are tridiagonal matrices. Meanwhile, the calculation of electric and magnetic field values in the three cartesian coordinate directions are independent of each other. Consequently, heterogeneous GPU parallel algorithms can be implemented to speed up the calculation as the calculation of field values in the three directions are independent of each other [42].

Similar to equation 36, we can rewrite equation 20 to the following equation with the direct splitting strategy:

$$\left(\mathbf{I}_6 - \mathbf{A}'\right)\left(\mathbf{I}_6 - \mathbf{B}'\right)\mathbf{W}^{n+1} = \left(\mathbf{C} + \mathbf{A}'\mathbf{B}'\right)\mathbf{W}^n + \mathbf{X}_1'\mathbf{M}_J^n + \mathbf{X}_2'\mathbf{M}_e^n + \mathbf{J}_s^{n+1}, \qquad (40)$$

where

$$\begin{cases} \mathbf{A}' = \begin{bmatrix} 0 & -a_1'\mathbf{R} \\ -d_0\mathbf{R}^T & 0 \end{bmatrix}, \mathbf{B}' = \begin{bmatrix} 0 & a_1'\mathbf{R}^T \\ d_0\mathbf{R} & 0 \end{bmatrix}, \\ \mathbf{C}' = \begin{bmatrix} a_0'\mathbf{I}_3 & 0 \\ 0 & \mathbf{I}_3 \end{bmatrix}, \mathbf{X}_1' = \begin{bmatrix} -a_2' & 0 \\ 0 & 0 \end{bmatrix}, \mathbf{X}_2' = \begin{bmatrix} a_3' & 0 \\ 0 & 0 \end{bmatrix}. \end{cases}$$

Therefore, equations 39a and 39b are rewritten as

$$\left(1 - a_1'd_0 D_{2(\varsigma-1)}\right)e_\varsigma^* = a_0'e_\varsigma^n - a_1'd_0 D_\varsigma D_{\varsigma-1} e_{\varsigma-1}^n \\ + a_1'D_{\varsigma+1} h_{\varsigma-1}^n - a_1'D_{\varsigma-1} h_{\varsigma+1}^n - a_2'M_{J_\varsigma}^n + a_3'M_{e_\varsigma}^n + j_{s_\varsigma}^{n+1}, \qquad (41a)$$

$$\left(1 - a_1'd_0 D_{2(\varsigma+1)}\right)e_\varsigma^{n+1} = e_\varsigma^* - a_1'd_0 D_\varsigma D_{\varsigma+1} e_{\varsigma+1}^*. \qquad (41b)$$

Equation 39c and equation 41 are the final full discretization of Maxwell's equations with CCM dispersion, which is named Caputo-BEDS algorithm in this paper.

Similar to what has been done in the Caputo-BEDS algorithm, we write equation 33 using matrices and add a higher-order error term to both sides of it to obtain the following equation:

$$\left(\mathbf{I}_6 - \mathbf{A}' - \mathbf{B}'\right)\mathbf{W}^{n+1} = \mathbf{C}''\mathbf{W}^n + \mathbf{X}_1''\mathbf{J}^n - \mathbf{X}_2''\mathbf{M}_J^n + \mathbf{X}_3''\mathbf{M}_e^n + \mathbf{J}_s^{n+1}, \qquad (42)$$

where

$$\mathbf{C}'' = \begin{bmatrix} a_0''\mathbf{I}_3 & 0 \\ 0 & \mathbf{I}_3 \end{bmatrix}, \mathbf{X}_1'' = \begin{bmatrix} -a_2'' & 0 \\ 0 & 0 \end{bmatrix}, \mathbf{X}_2'' = \begin{bmatrix} a_3'' & 0 \\ 0 & 0 \end{bmatrix}, \mathbf{X}_3'' = \begin{bmatrix} a_4'' & 0 \\ 0 & 0 \end{bmatrix}.$$

Thus, equation 41a can also be rewritten as:

$$\left(1 - a_1'd_0 D_{2(\varsigma-1)}\right)e_\varsigma^* = a_0''e_\varsigma^n - a_1'd_0 D_\varsigma D_{\varsigma-1} e_{\varsigma-1}^n + a_1'D_{\varsigma+1} h_{\varsigma-1}^n \\ - a_1'D_{\varsigma-1} h_{\varsigma+1}^n - a_2''j_\varsigma^n - a_3''M_{J_\varsigma}^n + a_4''M_{e_\varsigma}^n + j_{s_\varsigma}^{n+1}, \qquad (43)$$

The updating equations of the electric and magnetic fields can be obtained by combining equations 39c, 41b and 43. We refer to the algorithm discussed in this section as the SOE-BEDS algorithm which is illustrated in Algorithm 1.

Algorithm 1 3D forward with IP effects for SOE-BEDS

Initialize: fields value e_0, h_0, j_0
    Source current density j_s
    Auxiliary parameter $\mathbf{M}_j^0, \mathbf{M}_e^0$
    Calculate time steps Δt_n
do loop=1 →n
  !Saving field to calculate by (32)
  $AuxE_\zeta^n \leftarrow e_\zeta^{n-1}$
  $AuxJ_\zeta^n \leftarrow j_\zeta^{n-1}$
  !Calculating the virtual fields
  $e_\zeta^* \leftarrow e_\zeta^{n-1} \ h_\zeta^{n-1} \ M_{j_\zeta}^{n-1} \ M_{e_\zeta}^{n-1} \ j_v^{n-1}$ by (43)
  !Calculating the real fields
  $e_\zeta^n \leftarrow e_\zeta^*$ by (28b)
  !Calculating the current densities
  $j_\zeta^n \leftarrow e_\zeta^n \ j_\zeta^{n-1} \ M_{j_\zeta}^{n-1} \ M_{e_\zeta}^{n-1}$ by (28)
  !Calculating the auxiliary fields
  $U_{j_\zeta}^n, U_{e_\zeta}^n \leftarrow U_{j_\zeta}^{n-1} \ U_{e_\zeta}^{n-1} \ e_\zeta^n \ j_\zeta^n \ AuxE_\zeta^n \ AuxJ_\zeta^n \ s_v$ by (30) (31)
  ! There are $\mathcal{O}(2N_{exp})$ memory
  $M_{j_\zeta}^n, M_{e_\zeta}^n \leftarrow U_{j_\zeta}^n \ U_{e_\zeta}^n \ \xi_v$ by (29b)
  !Calculating the magnetic fields
  $h_\zeta^n \leftarrow h_\zeta^{n-1} \ e_\zeta^* \ e_\zeta^n$ by (39c)
end do

III. NUMERICAL EXPERIMENTS

A. The Verification of SOE Approximation

In the derivation of the SOE method in [32], the time-step sizes are assumed to be uniform (referred to as "uniform" type). In TEM simulations, however, the time-step sizes are required to be non-uniform for efficiency considerations. For example, smaller time steps are required to accurately capture the rapidly changing EM fields in early times. At later times, larger time steps are more appropriate and can reduce the computation time significantly. Um et al. [50] consider a fixed time step size for all steps within one section comprising a certain number of steps and used an automatic procedure to double the time step in the next section (referred to as "linear" type). Oldenburg et al. [51] divide the modeling time into P sections, each of which has a constant time step that is increasing with a predefined rate from early to late sections (referred to as "non-uniform" type). To verify the accuracy of the SOE-BEDS algorithm with different time-stepping schemes, we compare the current density calculated by the $L1$ approximation method and the SOE approximation method (equations 18 and 28, respectively). We analyze the relative errors between both methods. The 46466 random electric field values are used as inputs to the current density formula (equations 3). Several results are shown in Figure 2a-2c, which include three cases: 1) different step interval types, 2)

different CCM exponents, and 3) different uniform absolute errors. The non-uniform step-sizes are adopted in case 2 and case 3 and the parameters are listed in Table 1. The relative error between the results calculated by $L1$ approximation and SOE approximation methods in Figure 2d-2f.

For case 1, the purpose is to consider the effect of time-stepping schemes on SOE method as shown in Figure 2a. For the "uniform" type, the step size is set to 1.15×10^{-7}s. For the "linear" type, the step size increase from 1.3×10^{-7}s to 3.31×10^{-7}s and the growth factor is 1.00002. The step value with P subintervals is adopted in the "non-uniform" type, in which the minimum step size is 1.0×10^{-9}s and maximum step size is 1.8×10^{-5}s. From Figure 2d, we can see that the relative errors are within 1%, with the "linear" and "non-uniform" types exhibiting relative errors less than one part per million (the top left of Figure 2d). However, the errors of all curves linearly increase with time, and there is an increase in the level of fluctuation.

The CCM exponent is a crucial factor in the behavior of dispersive mediums. For Case 2, five values are considered (Figure 2b). From Figure 2e, the relative errors stay below 4%. Clearly, the errors become smaller as c increases. The relative error also increases almost linearly with time, with the level of fluctuation increasing as well.

Finally, the curves of relative errors with different uniform absolute errors are shown in Figure 2f for case 3. When δ is set to 0.1, the amplitude of change in the relative error curve gradually increases. Furthermore, at later times, the value of error exceeds 5%. However, the relative error remains relatively stable within 1% as δ are set to $1e^{-3}$, $1e^{-6}$, and $1e^{-9}$ respectively. We should note that the relative error corresponding to $\delta=1e^{-9}$ is not the smallest when the non-uniform time-stepping scheme is used. However, the calculational accuracy is acceptable for $\delta < 1e^{-9}$ when we obtain the nodes and weights for n-point Gauss-Legendre quadrature. In general, the relative error of the SOE approximation method will increase over time for all cases considered here. Also, it is obvious that the non-uniform time-stepping scheme and $\delta = 1 \times 10^{-3}$ give smallest relative error, and they are used for the remaining modeling examples in this paper

After the above analyses about the three cases which compares the performance of the $L1$ approximation and the SOE approximation, we conclude that the SOE approximation is yields very close results as those from the $L1$ approximation and is therefore a valid method to be considered in the calculation of the fractional differential equation. Note that N_{exp} will be obtained when β, δ, ϑ and t are input into equation 24. However, N_{exp} has been kept small for all the cases listed in Table I.

B. Accuracy Verification

To verify the accuracy of the SOE-BEDS method, we first consider a homogeneous half-space model as shown in Figure 3 and compare the calculated vertical component of $d\mathbf{b_z}/dt$-field with that of Seidel and Tezkan [52]. The Cole-Cole

parameters for the half space are σ_∞=0.02S/m, η=0.5, c=0.5, and τ=0.001s. The transmitter size is 50m by 50m. The transmitter and receiver are placed on the ground surface. The size of loop is 50m by 50m, and the current in the transmitter is set to 1 A. The model is discretized with $101\times101\times100$ grids. The grid spacing is uniform within the core region which contains the source and receiver. The cell size is

enlarged gradually away from the core region. The smallest size of grid is 10m. The conductivity σ_{air} and σ_{ground} are set to 0.02S/m and 1e-6S/m respectively. Figure 4 shows the decay curves calculated using the SOE-BEDS algorithm presented in this paper and from [52]. We can see that the two curves have a good match over most of the modelling time range.

TABLE 1
PARAMETERS FOR FRACTIONAL DERIVATIVE APPROXIMATION

Project	CCM exponent c	Uniform absolute error δ	Step interval type	N_{exp}
Case 1	0.5	10^{-9}	uniform/linear/non-uniform	63/64/82
Case 2	0.1/0.3/0.5/0.7/0.9	10^{-9}	non-uniform	80/81/82/83/84
Case 3	0.5	$10^{-1}/10^{-3}/10^{-6}/10^{-9}$	non-uniform	15/33/58/82
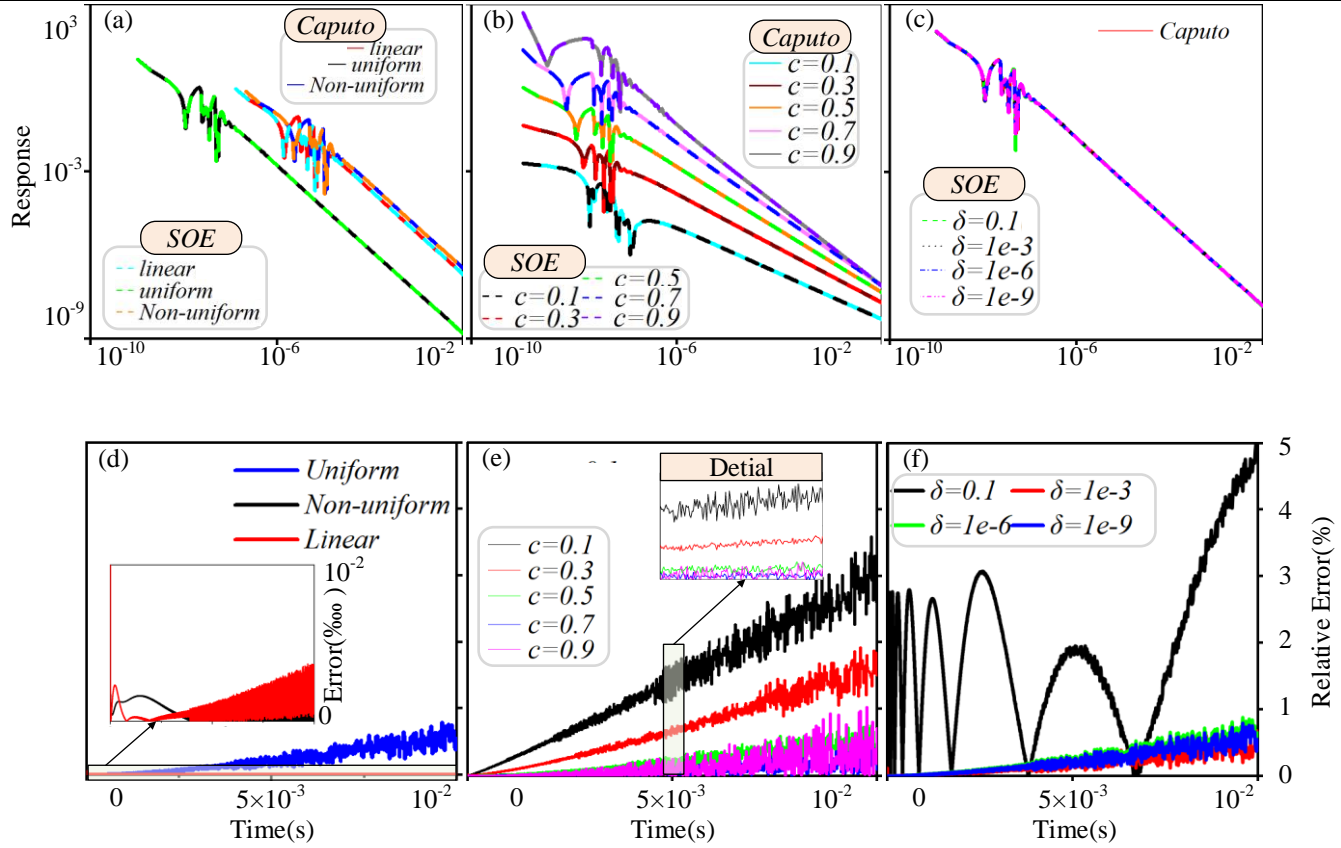
Fig. 2. Comparison of current density for L1-approximation and SOE-approximation method in different parameters within 10^{-2}s. (a) Responses in different step interval types. (b) Responses in different CCM exponents. (c) Responses in different uniform absolute errors. (d) Relative errors in different step interval types. (e) Relative errors in different CCM exponents. (f) Relative errors in different uniform absolute errors.
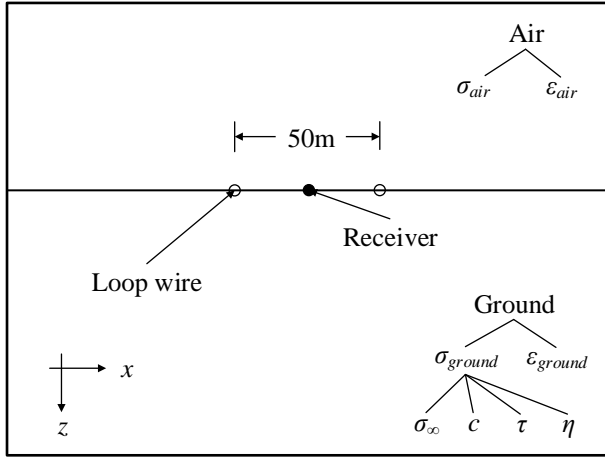
Fig. 3. The schematic diagram of a homogeneous half-space model. The solid dots are used as the transmitting source and the receiver is placed at the center of the loop (hollow dot).
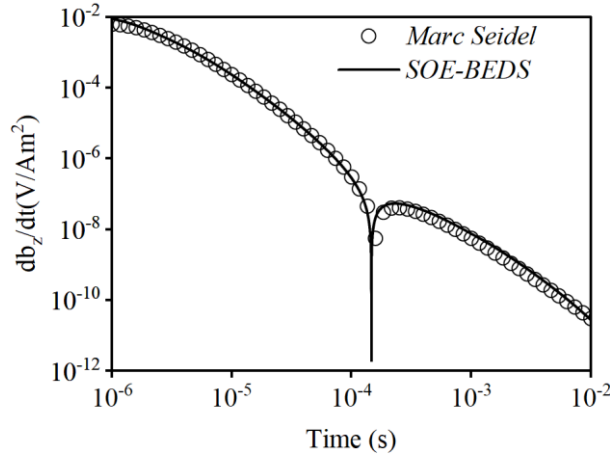

Fig. 4. The decay curves calculated by the SOE-BEDS method for the model given in Fig.2 (solid line) and from [52] (hollow circle).
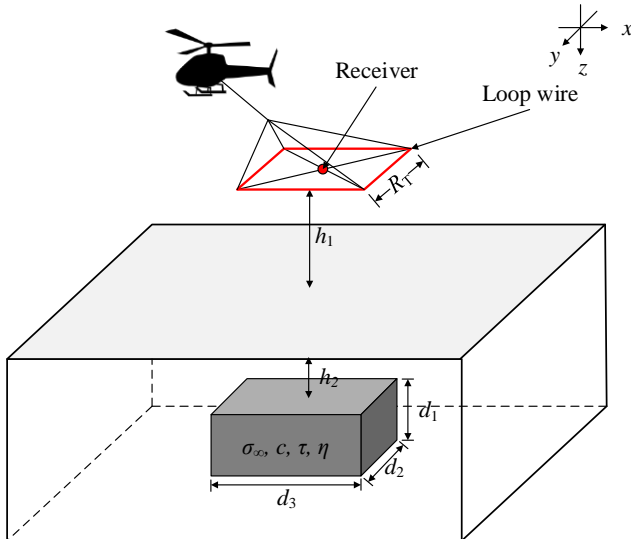

Fig. 5. Diagram of a chargeable block buried in a homogeneous half space.
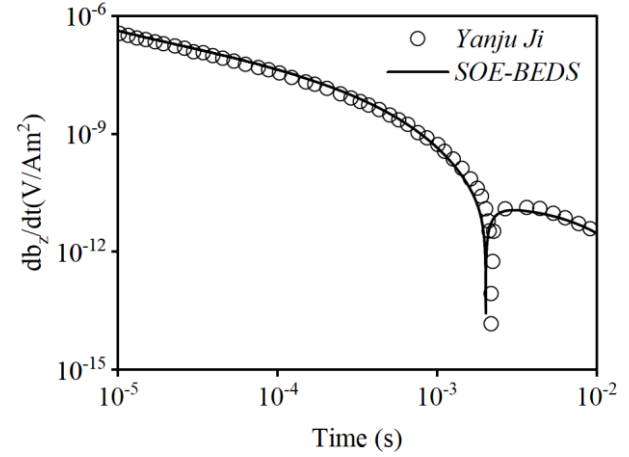The red square loop denotes the transmitter location. The red dot denotes the receiver location.

Fig. 6. Comparison of 17.5m × 17.5m coincident-loop transient responses to chargeable block in a half-space model using SOE-BEDS method and [28].

Next, we verify the accuracy of the SOE-BEDS algorithm using a model comprising an anomalous chargeable body buried in a homogeneous half space (Figure 5). The CCM parameters of the block are set to $\eta=0.2$, $\tau=0.005$s and $c=1.0$. The conductivity of the ground, the air, and the chargeable body are set to 1e-3S/m 1e-6S/m, and 1e-1S/m respectively. The dimensions of the chargeable body are set to $d_1=200$m and $d_2=d_3=250$m, respectively. The distance between the top of the block and the ground is $h_2=50$m. We use a square loop wire frame to approximate a circular, $R_T=17.5$m and $h_1=30$m. The transmitter current is set to 1.538A. We discretize the model with 201 × 201 × 200 grids. The region containing the chargeable body is discretized with 10 ×10 ×10m uniform grids. The decay curve calculated by our SOE-BEDS algorithm and by [28] are shown in Figure 6, and the two decay curves agree well. The sign reversal caused by the IP effect can be clearly seen in both curves.

C. Computational Efficiency Analyses

To compare the computational efficiency of SOE-BEDS and Caputo-BEDS methods, we consider the homogeneous half-space model (Figure 3) and carry out the forward modeling using a Linux workstation equipped with an NVIDIA RTX A6000 GPU and an AMD EPYC 7742 CPU. A trapezoidal waveform is considered for the source in Figure 7 [53]. During the turn-on and turn-off stages, the time-step sizes are fixed at 1e-9s. Considering the non-derivable points in trapezoidal waveform, the switching function is used to smooth the rising and the ramp edge, respectively [53]. To shorten the simulation time, the time-step sizes are not uniform throughout the steady stage. It increases from 1e-9s until it reaches 1.2e-4 s at the middle of the steady stage. Then, it starts to decrease and stops at 1e-9 s at the end of the steady stage.

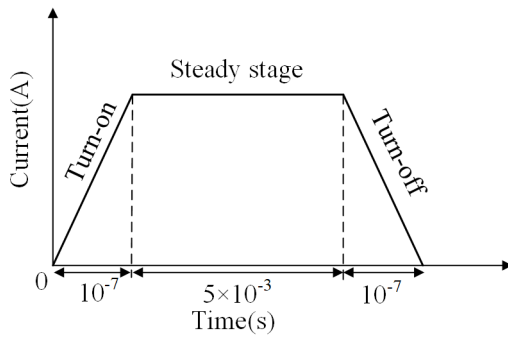> REPLACE THIS LINE WITH YOUR MANUSCRIPT ID NUMBER (DOUBLE-CLICK HERE TO EDIT) <

Fig. 7. Schematic diagram of the trapezoidal transmitting current waveforms.

The parameters of the CCM model are c=0.5, η=0.5, and τ=0.0001s. The value of σ_∞ is set to 0.1S/m. The conductivity of the air is set to 1e-6S/m. The permittivity of the air and the half-space background is set to that of free air [54]. We discretize the model with $35 \times 35 \times 40$ cells. The strategy of non-uniform grid spacing is adapted. Yu et al. [55] suggested the ratio between two adjacent cells should be less than 1.2. although the central difference method for non-uniform grid only keeps first-order accuracy, the accuracy of the result is satisfying. The core region which contains the source and receiver is discretized with $10 \times 10 \times 10$m uniform grids. There are 18733 time steps in the entire simulation, including 100 on-time and off-time time steps respectively.

The db_z/dt-field responses of the half-space model calculated with the Caputo-BEDS method (red solid line) and with the SOE-BEDS method (black dotted line) are shown in Figure 8. The two curves match well with each other throughout the entire time range modeled. The relative errors are all below 5% from 10^{-5}s to 10^{-3}s, except for the time when the negative responses appear.
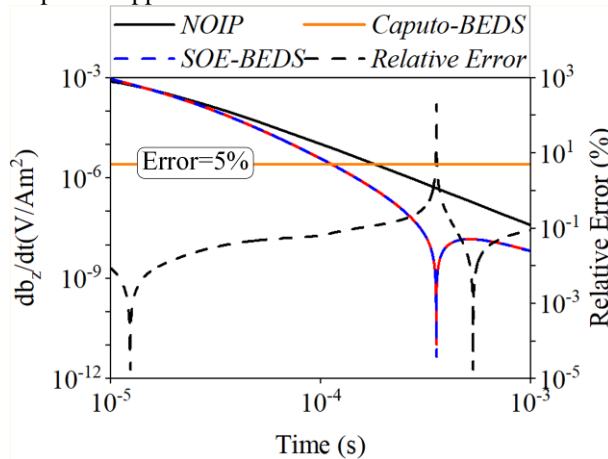

Fig. 8. The forward modeling results calculated by the Caputo-BEDS method (red solid line) and the SOE-BEDS method (blue dashed line), and the relative error between the two methods (black dashed line). The db_z/dt-field response calculated without considering the IP effect is plotted with the black solid line.

Another noteworthy aspect is that the Caputo-BEDS method requires 43.77G of memory and takes 15.14h to complete the forward modeling calculation, but the SOE-

BEDS method only took 44.18s and consumed 831M of memory. To illustrate the reason for this significant difference, we plotted the calculation time required for each step by both methods in Figure 9.
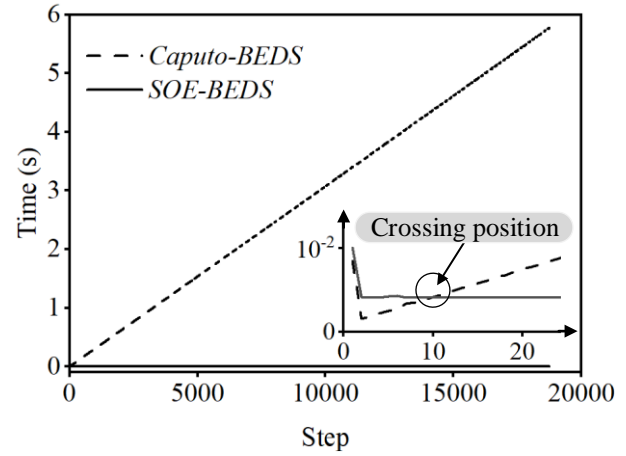

Fig. 9. The calculation time required to finish a single forward modeling iteration by the Caputo (dotted line) and the SOE methods (solid line).

It is evident that the time that the SOE method consumed for each step remains constant during the entire simulation. In contrast, the time required by the Caputo method for each step is linearly increasing with iteration steps (except for the first two steps), although it is shorter than that of the SOE method for the first 10 steps.

D. Characteristics Analyses of TEM Responses with Different Polarization Parameters

Different IP parameters of the CCM can result in different TEM responses. We design some examples to obtain the applicability with different CCM parameters by comparing the results calculated by SOE-BEDS and Caputo-BEDS method. The results are shown in Figure 10. We consider central loop configuration with a rectangular loop of 50m, and the transmitter current is set to 1A. We first consider a homogeneous half-space model and set σ_∞ of the chargeable half space to 0.1S/m. We consider three groups of modeling where we only change one CCM parameter and keep the other two fixed: 1) different CCM exponents, 2) different chargeability, 3) different central relaxation time constants. The specific values of the CCM parameters for the 12 models modeled are listed in Table 2.

The db_z/dt-field response without considering the IP effect, as well as the db_z/dt-field response of models considering the IP effects calculated using the Caputo-BEDS and SOE-BEDS methods are shown in Figure 10. An excellent agreement between the results calculated by the two methods is obtained for all models. Three types of responses are observed with different combinations of c, τ, and η: *"no sign reversal"* (Figure 10i) *"single sign reversal"* (Figure 10f) and *"double sign reversals"* (Figure 10d). The relative error exceeds 5% around times when the sign reversal occurs.

We can see that c affects the time when the sign reversal happens and the number of time reversal occurrences (Figure

10a-10d). A larger value of c would cause the sign reversal to happen earlier. A second sign reversal is found to exist in the decay curves for all c values but at much later times for small c values, and hence not plotted in panels (a), (b), and (c). Having a large c causes the second sign reversal to appear within the modeled time range. On the contrary, when c decreases, the decay curve becomes more similar to that without the IP effect. In the extreme case of $c=0$, the electrical conductivity stops being dispersive, and the decay curve would become the same as the one without considering IP effect.

The chargeability η affects the decay curve in a similar way as c. A larger η would cause the time reversal to occur earlier. However, there remains to be only one sign reversal with large values of η ($\eta = 0.9$). When $\eta=0$, equation 2 reverts to Ohm's law without dispersion.

The central relaxation time τ determines the length of time required for the decay in the time domain. When $\tau=0$, $\sigma(t)=\sigma_0$ [56] which implies the medium is no longer dispersive, and therefore. Consequently, the d$\mathbf{b_z}$/dt-field responses of loop center remain constantly positive. Similarly, according to equation 1, $\sigma(t)=\sigma_\infty$ when $\tau=\infty$. The model is charged all the time. Thus, the d$\mathbf{b_z}$/dt-field response of loop center remains the same as the TEM response without the IP effect. With τ decreasing, the model has less time for charging then discharges earlier, which results in appearance of negative responses in Figure 10i-10l.

According to the definition of the Cole-Cole model (equation 1), we can deduce that the changes for different parameters only have an impact on the complex electrical resistivity. The time-variant resistivity expression for Cole-Cole model can be obtained by using the inverse Laplace transform [57]:

$$\rho(t) = L^{-1}\left[\rho(\omega)\right] = \frac{\rho_0}{1-\eta}\left\{1-\eta L^{-1}\left[1-\frac{1}{1+(s\tau)^c}\right]\right\}. \quad (44)$$

Using the digital filter algorithm of [19], equation 44 can be expressed as

$$\sigma(t) = \frac{1}{\rho(t)} = \sigma_0\frac{1-\eta}{1-\eta\sum_{k=1}^{21}\varphi_k \text{Re}(\omega_k)}, \quad (45)$$

where $Re(\omega_k)$ is the real part of the expression $(1-1/(1+(i\omega\tau))^c)$ and is defined as

$$\text{Re}(\omega_k) = \left(1-\frac{1+(\omega_k\tau)^c\cos\frac{\pi c}{2}}{1+(\omega_k\tau)^{2c}+2(\omega_k\tau)^c\cos\frac{\pi c}{2}}\right).$$

In equations 45, $\omega_k=10^{\alpha_k}/t$, where α_k is filtering calculation node and φ_k is the filter coefficient. We can obtain the electrical conductivity curves with various IP parameters in Figure 11.

Although different parameters (c, η, and τ) both affect the time when the sign reversal occurs, the causes are different. The electrical conductivity decreases with time from σ_0 (the upper limits) to σ_∞ (the lower limits) in each panel. Meanwhile,

when the electrical conductivity is equal to a constant, the phenomenon of sign reversal doesn't occur. So, we conclude it is the change between σ_0 and σ_∞ with time that causes the alternating positive and negative d$\mathbf{b_z}$/dt-field responses. The slope of curve at any given time represents the rate of change from σ_0 to σ_∞ at that time.

The slop of the curve is positively correlated with c in Figure 11a. The electrical conductivity linearly decreases with time when c is small enough. Therefore, the negative response appears later with smaller c as seen in Figure 10a. The smaller chargeability value not only decreases the slope, but also the electrical conductivity is close to a constant in Figure 11b. Thus, the TEM response is similar to the response without the IP effect, and no sign reversal occurs in Figure 10e. Different central relaxation times have no effect on the shape of the conductivity curve, but the time at which the conductivity starts to change from σ_0 to σ_∞ becomes later as τ increases (Figure 11c). So, a large τ also causes the occurrence of negative responses to appear later in time.

To explore the influence of high-frequency electrical conductivity σ_0 on electromagnetic response, four half spaces with five different conductivities: $\sigma_0=0.01$S/m, 0.005S/m, 0.0025S/m, 0.00167S/m, and 0.00125S/m. We consider a half-space model with the same survey configuration as shown in Figure 3. The results are shown in Figure 12. According to [58], the total field includes fundamental field and polarization field. The fundamental field is stronger under high electrical conductivity, which overpowers the polarization field in the late stages. So, the sign reversal happens earlier when σ_∞ decreases. Further, the sign reversed twice within the modeling time range as σ_∞ decreases to 0.0025 S/m.

E. Characteristics Analyses of TEM Responses with A 3D Chargeable Body in A Nonchargeable Half space

To further study how the TEM responses change with time when a chargeable body is present, we consider, again, the model with 3D chargeable body buried in nonchargeable half space (Figure 5). The transmitter and receiver are placed on the ground surface, $h_1=0$. The size of the chargeable body is $d_1=100$m, $d_2=d_3=210$m, and $h_2=50$m. The transmitter current is set to 1A. The model is discretized with $81\times81\times80$ grids. The conductivity σ_{ground} is set to 0.02S/m. we prepare three models: Case1: homogeneous half-space model ($\sigma_\infty=0.02$S/m,), Case2: containing nonchargeable low-resistance body ($\sigma_\infty=0.1$S/m), and Case3: containing chargeable low-resistance body ($\sigma_\infty=0.1$S/m, $\eta=0.5$, $\tau=0.001$s, $c=0.5$).

The responses of the d$\mathbf{b_z}$/dt-field at the receiver are shown in Figure 13. We turn attention on the results of Case3, the red dashed line curve in Figure 13. Comparing the results of Case2, the decay curve appears the difference near 0.22ms and the sign reversal is observed near1.31ms. Both decay curves coincide from 0.01ms to 0.22ms, as well as the response value increases due to the presence of the underground conductive body. After $t = 0.22$ms, the amplitude decreases rapidly under the influence of IP effects.

TABLE 2
PARAMETERS FOR FORWARD MODEL

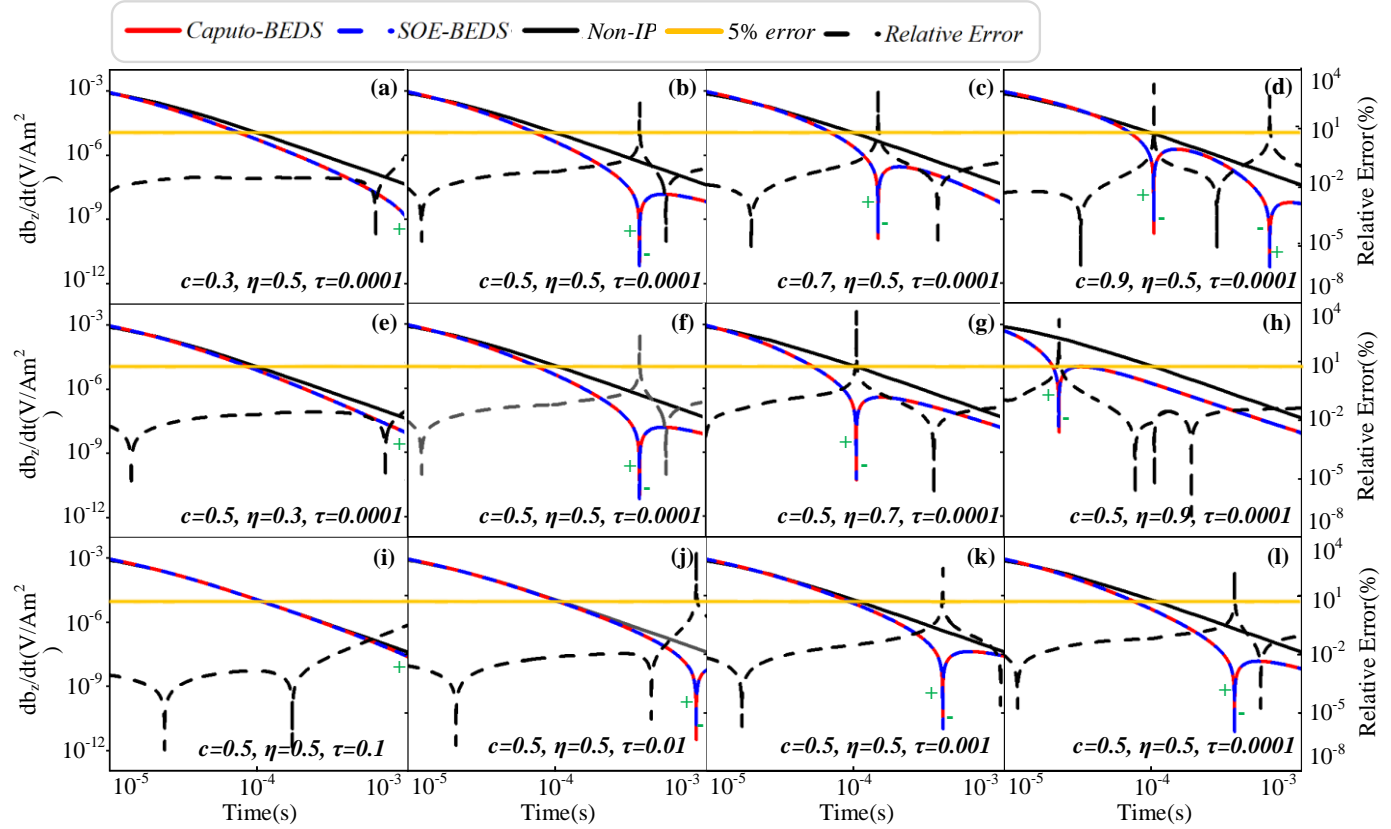| Group	CCM exponent c	Chargeability η	Central Relaxation Time $\tau(s)$
Case 1	0.3/0.5/0.7/0.9	0.5	0.0001
Case 2	0.5	0.3/0.5/0.7/0.9	0.0001
Case 3	0.5	0.5	0.0001/0.001/0.01/0.1

Fig. 10. The d$\mathbf{b_z}$/dt-field responses calculated for the 12 models with different CCM parameters listed in Tabel 2 by the Caputo-BEDS (red solid line) and SOE-BEDS (blue dashed line) methods. The yellow horizontal line in each panel represents 5% relative error. The TEM response without the IP effect is shown with dark gray solid lines in each panel. The relative error between the responses calculated by the two numerical methods is shown with black dashed lines in each panel.
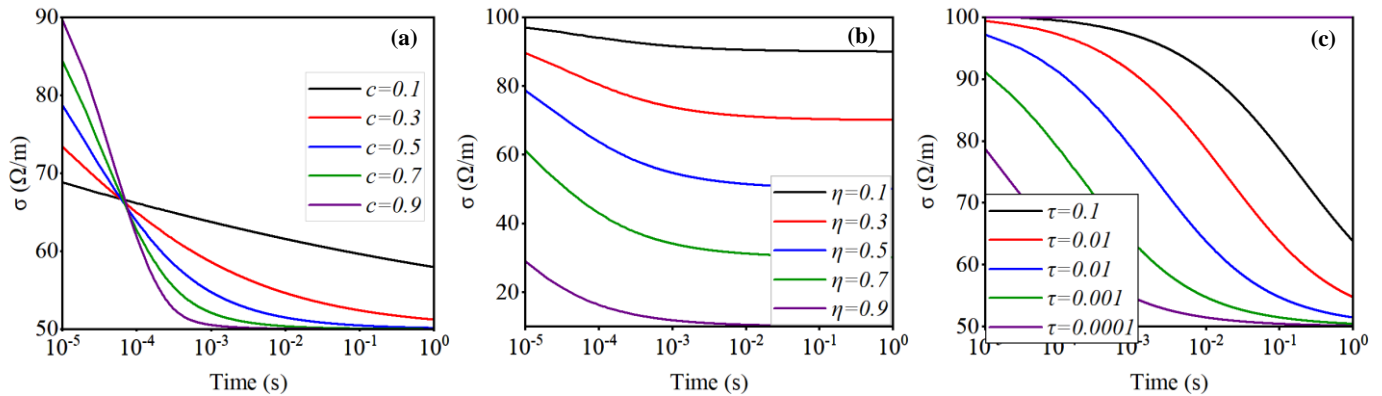

Fig. 11. Comparison of the electrical conductivity with different IP parameters.
(a) Different CCM exponents, c=0.1, 0.3, 0.5, 0.7, 0.9. (b) Different chargeability, η=0.1, 0.3, 0.5, 0.7, 0.9.
(c) Different relaxation time constants, τ=0.0001s, 0.001s, 0.01s, 0.1s, 1s.

This article has been accepted for publication in IEEE Transactions on Geoscience and Remote Sensing. This is the author's version which has not been fully edited and content may change prior to final publication. Citation information: DOI 10.1109/TGRS.2024.3383388

1

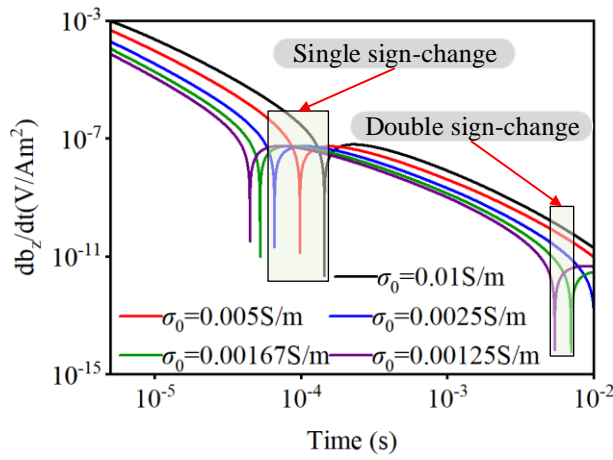> REPLACE THIS LINE WITH YOUR MANUSCRIPT ID NUMBER (DOUBLE-CLICK HERE TO EDIT) <

Fig. 12. The d$\mathbf{b_z}$/dt-field responses with different electrical conductivity for SOE-BEDS method. Other CCM parameters are set to c=0.5 and η=0.5.
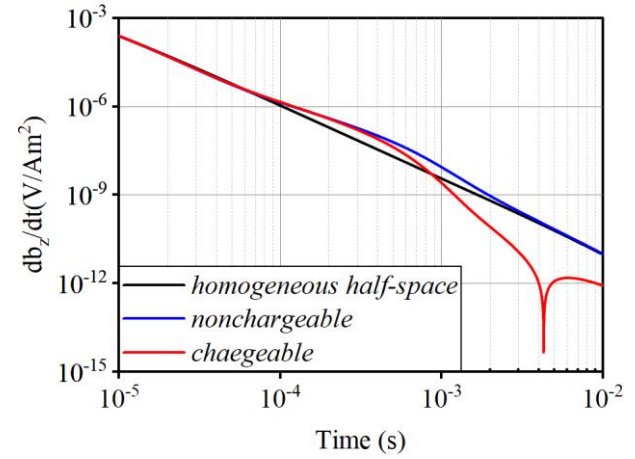
Fig. 13. Decay curves of the d$\mathbf{b_z}$/dt-field responses with nonchargeable body (blue dotted line), chargeable body (red dashed line), and homogeneous half-space model (black solid line).
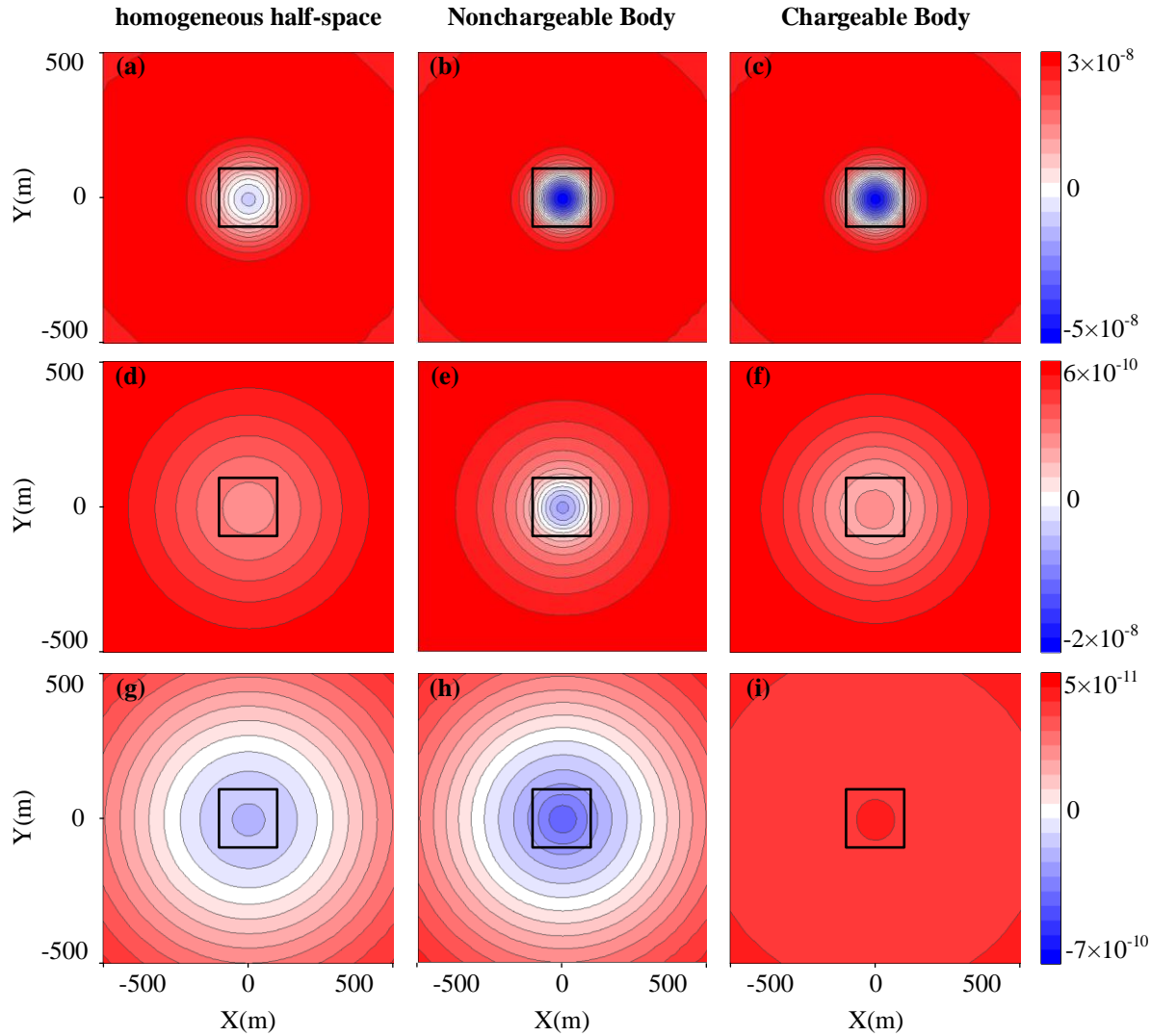

Fig. 14. The response maps of d$\mathbf{b_z}$/dt-field on the surface and the time channels are 0.18ms (a)-(c), 0.88ms (d)-(f) and 5.54ms (i)-(k). From left to right, homogeneous half-space model, the anomalous with nonchargeable low resistance body and chargeable low resistance body are shown by black frame.
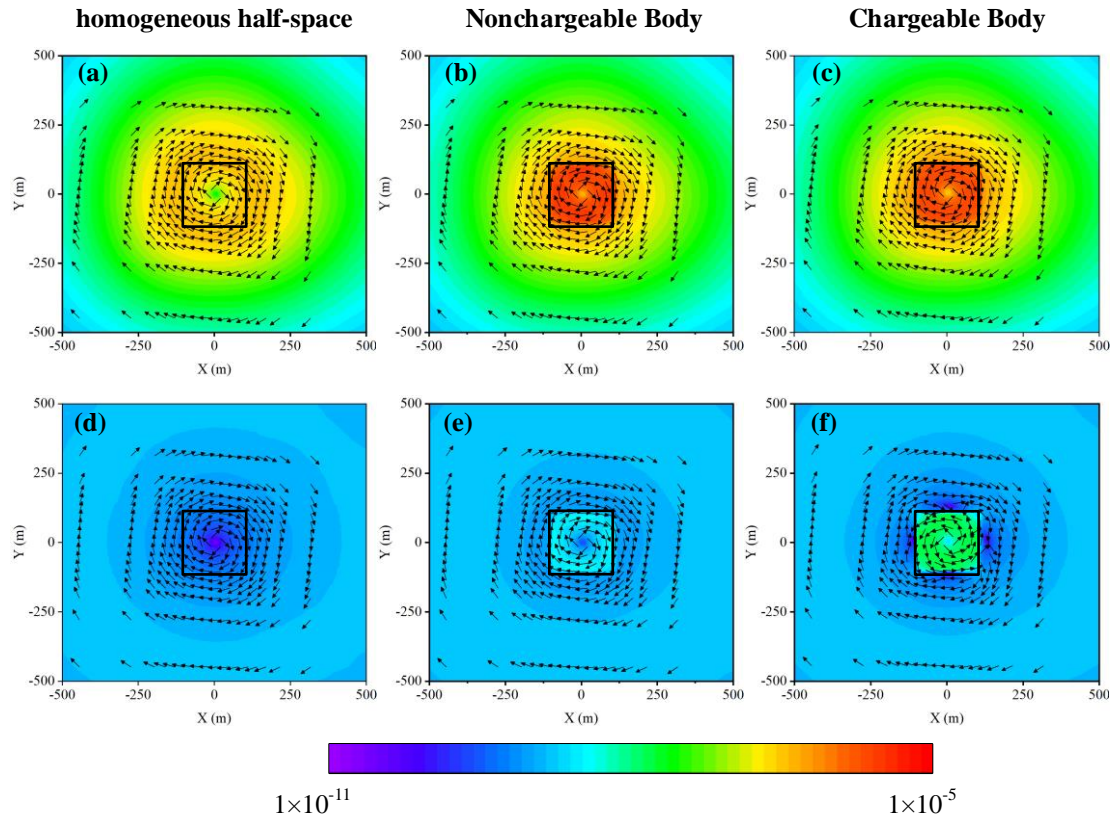
Fig. 15. The maps of current density and section views at 100m depth. The time channels are 0.18ms (a)-(c) and 5.54ms (d)-(f). From left to right, homogeneous half-space model, the anomalous with nonchargeable low resistance body and chargeable low resistance body are shown by black frame. Black arrows and coloured background respectively indicate the direction and amplitude of the current.
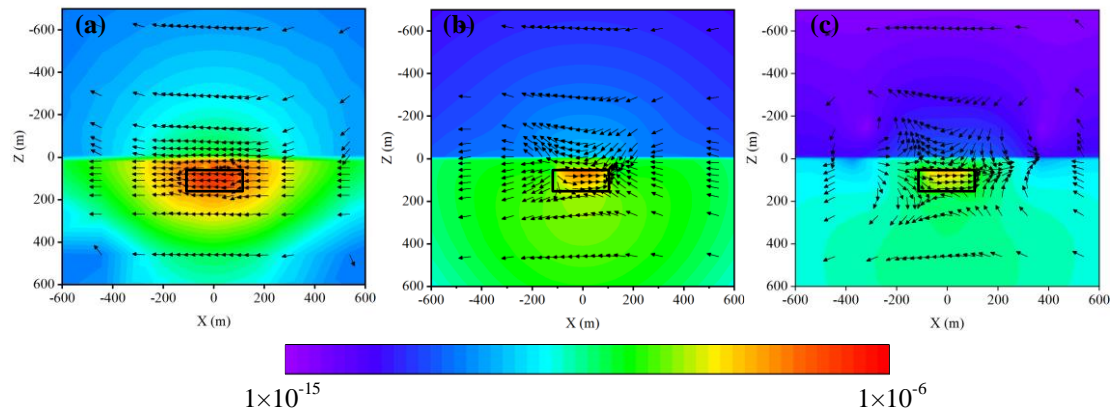

Fig. 16. The maps of current density of the model with chargeable body shown by black frame and section views at XOZ. The time channels are 0.18ms (a), 0.88ms(b) and 5.54ms (c). Black arrows and coloured background respectively indicate the direction and amplitude of the current.

The decay curves shown in Figure 13 show how the $d\mathbf{b_z}/dt$ field is changing with time at the observation point. We focus on the $d\mathbf{b_z}/dt$-field responses on the surface with three times channels. Figure 14 shows contour maps at 0.18ms, 0.88ms and 5.54ms. We note that the results are similar between the model with the nonchargeable low-resistance body and chargeable low-resistance body at 0.18ms. In Figure 14b and 14c, the negative responses are concentrated inside the position of black frame. at 0.18ms. This phenomenon indicates that the polarizable anomalous body is probably still charging. Observing Figure 14a and 14b, the responses within black frame are smaller due to the influences of low-resistance body, which phenomenon is the same as shown in Figure 13.

Then at 0.88ms, it is clearly that the chargeable body has a noticeable effect on the results in Figure 14f, and we observe the positive results inside the loop. However, the responses are negative at same position in Figure 14e. We conclude that the polarizable anomalous body is discharging. This phenomenon can be explained by the fact that the polarization current resulted from IP effect is the opposite to the conduction current. With the increase in time, the amplitude of the $d\mathbf{b_z}/dt$-field responses continuously increase, as seen in Figure 14i.

At 5.54ms, strong IP effects can be observed because the observed data already show signal reversal. Meanwhile, the smoke ring effect is also evident through the response diffusion phenomenon with the time. Conversely, utilizing the IP effect at different times can prove to be highly helpful in exploring low-resistance bodies. This insight underscores the potential advantages of leveraging the IP effect for improved exploration of subsurface structures.

To understand what is happening physically for the IP effects inside the anomalous body, we plot the current density at the XOY plane at a depth of 100m in Figure 15 at 0.18ms and 5.54ms. The black arrows represent the current direction and the background color represent the amplitude of the current.

The current density inside and outside the anomalous body is clockwise at 0.18ms, but the amplitude of the current density inside the anomalous body in Figure 15b and 15c is larger than that shown in Figure 15a. The larger amplitude is the influence of low resistance body. The amplitude of body without the IP effect is greater than one with IP effect, indicating that the chargeable body is probably being charged at early times. At the later time when t = 5.54ms, it can be seen that the current density inside the chargeable body reverses its direction to counterclockwise as opposed to clockwise at t = 0.18ms. The direction change is not observed for the other two models at t = 5.54ms. This direction change for current density in the anomalous body is likely caused by the discharging of the chargeable body.

The current density is also plotted for the XOZ plane cutting through the middle of the chargeable body in Figure 16. At early times when t = 0.18ms, the current density direction is generally the same inside and outside the chargeable body. Then a reverse current is formed inside body at 0.88ms and 5.54ms. The current direction around body is complicated due to the influence of low resistance and IP effects.

IV. CONCLUSION

In this paper, we present a novel technique for modeling the TEM responses when the model contains chargeable materials. We developed the SOE method to approximate the Caputo function rather than using a linear interpolation to solve fractional derivatives in Ohm's law. The results of current density calculated by SOE method show that SOE method can effectively and accurately approximate Caputo function with non-uniform step-size.

Then Caputo functions approximated by linear interpolation and SOE methods are introduced into the Maxwell equation adopting the finite difference (FD) and backward Euler's (BE) to establish Caputo-BEDS and SOE-BEDS algorithms. The results from both methods show that the algorithm we developed has higher accuracy expect for the region with field changing, which relative error is less than 5%. It should pay attention to which the SOE-BEDS algorithm significantly reduces computation time, measured in seconds rather than hours. Meanwhile, it only occupies lower memory under the same model.

For various IP parameters in the model, the results show that the Caputo-BEDS and SOE-BEDS methods keep high precision. By exploring electromagnetic response maps of models containing anomalous bodies, it is demonstrated that the IP effect is more particularly advantageous for detecting subsurface anomalies.

We hope that this method can provide an efficient and accurate computational basis for IP interpretation.

APPENDIX

A1 Derivation for discretizing the fractional derivatives

We restate the Caputo approximation function for fractional derivatives:

$$\frac{\partial^c f(t_n)}{\partial t^c} = \frac{1}{\Gamma(1-c)} \int_0^{t_n} \frac{f'(m)}{(t-m)^c} dm. \tag{A1}$$

In $[t_p, t_{p+1}]$, we take the approximation $\dot{f}(m) = [f(t_{p+1}) - f(t_p)]/\Delta t_p$, then substitute into equation A1 obtains

$$\frac{1}{\Gamma(1-c)} \int_0^{t_n} \frac{f'(m)}{(t-m)^c} dm = \frac{1}{\Gamma(1-c)} \sum_{p=0}^{n-1} \frac{f(t_{p+1}) - f(t_p)}{\Delta t_p} \int_{t_p}^{t_{p+1}} \frac{1}{(t_n-m)^c} dm. \tag{A2}$$

The integration by parts is used, we can obtain

$$\int_{t_p}^{t_{p+1}} \frac{1}{(t_n-m)^c} dm = \frac{1}{1-c}(t_n-m)^{1-c}\Big|_{t_{p+1}}^{t_p}. \tag{A3}$$

Then, equation A2 becomes

$$\frac{1}{\Gamma(1-c)} \int_0^{t_n} \frac{f'(m)}{(t-m)^c} dm$$

$$= \frac{1}{\Gamma(1-c)} \frac{1}{1-c} \sum_{p=0}^{n-1} \frac{f(t_{p+1}) - f(t_p)}{\Delta t_p}\Big[(t_n-t_p)^{1-c} - (t_n-t_{p+1})^{1-c}\Big], \tag{A4}$$

where Γ is the Gamma function and is expressed as

$$\frac{1}{\Gamma(z)} = \int_0^\infty t^{z-1}e^{-t}dt.\Re(z) > 0 \tag{A5}$$

Assuming $z=1-c$, equation A5 can be expressed as

$$\frac{1}{\Gamma(1-c)}\frac{1}{1-c} = \frac{1}{1-c}\int_0^\infty t^{-c}e^{-t}dt = \int_0^\infty e^{-t}dt^{1-c} = \int_0^\infty t^{1-c}e^{-t}dt$$

$$= \frac{1}{\Gamma(2-c)}.\Re(c) < 1 \tag{A6}$$

Expanding the summation formula gives

$$\sum_{p=0}^{n-1} \frac{f(t_{p+1})-f(t_p)}{\Delta t_p}\Big[(t_n-t_p)^{1-c}-(t_n-t_{p+1})^{1-c}\Big]$$

$$=\frac{f(t_1)-f(t_0)}{\Delta t_0}\Big[(t_n-t_0)^{1-c}-(t_n-t_1)^{1-c}\Big]$$

$$+\frac{f(t_2)-f(t_1)}{\Delta t_1}\Big[(t_n-t_1)^{1-c}-(t_n-t_2)^{1-c}\Big] \quad (A7)$$

$$+...$$

$$+\frac{f(t_n)-f(t_{n-1})}{\Delta t_{n-1}}\Big[(t_n-t_{n-1})^{1-c}-(t_n-t_{n-2})^{1-c}\Big].$$

Rearranging equation A7, we have

$$\sum_{p=0}^{n-1} \frac{f(t_{p+1})-f(t_p)}{\Delta t_p}\Big[(t_n-t_p)^{1-c}-(t_n-t_{p+1})^{1-c}\Big]$$

$$=-\Big[(t_n-t_0)^{1-c}-(t_n-t_1)^{1-c}\Big]\frac{f(t_0)}{\Delta t_0}$$

$$-\left\{\frac{\Big[(t_n-t_1)^{1-c}-(t_n-t_2)^{1-c}\Big]}{\Delta t_1}-\frac{\Big[(t_n-t_0)^{1-c}-(t_n-t_1)^{1-c}\Big]}{\Delta t_0}\right\}f(t_1)$$

$$-...$$

$$-\left\{\frac{\Big[(t_n-t_{n-1})^{1-c}-(t_n-t_{n-2})^{1-c}\Big]}{\Delta t_{n-1}}-\frac{\Big[(t_n-t_{n-2})^{1-c}-(t_n-t_{n-3})^{1-c}\Big]}{\Delta t_{n-2}}\right\}f(t_{n-1})$$

$$+\Big[(t_n-t_{n-1})^{1-c}-(t_n-t_{n-2})^{1-c}\Big]\frac{f(t_n)}{\Delta t_{n-1}}.$$

$$(A8)$$

Allowing the final in equation A8 is written as

$$\sum_{p=0}^{n-1}\frac{f(t_{p+1})-f(t_p)}{\Delta t_p}\Big[(t_n-t_p)^{1-c}-(t_n-t_{p+1})^{1-c}\Big]$$

$$=\frac{b_{n-1}^n}{\Delta t_{n-1}}f(t_n)-\sum_{p=1}^{n-1}\left(\frac{b_p^n}{\Delta t_p}-\frac{b_{p-1}^n}{\Delta t_{p-1}}\right)f(t_p). (n\geq 2) \quad (A9)$$

Substituting equation A9 and A6 into equation A4, equation A1 can be rewritten as

$$\frac{\partial^c f(t_n)}{\partial t^c}=\frac{1}{\Gamma(2-c)}\left[\frac{b_{n-1}^n}{\Delta t_{n-1}}f(t_n)-\sum_{p=1}^{n-1}\left(\frac{b_p^n}{\Delta t_p}-\frac{b_{p-1}^n}{\Delta t_{p-1}}\right)f(t_p)\right]. \quad (A10)$$

A2 Derivation for discretizing Integral part of equation 31

We first compute the $f(m)$ via linear function. Assuming the field is $f(\tau)$ at τ time, the expression can be written as the following range from t_{n-1} to t_n:

$$\frac{f(t_n)-f(\tau)}{t_n-\tau}=\frac{f(t_n)-f(t_{n-1})}{t_n-t_{n-1}}. \quad (A11)$$

Substituting into equation 30, we get

$$\int_{t_{n-1}}^{t_n} e^{-s_i(t_{n+1}-\tau)}\left[\frac{f(t_n)-f(t_{n-1})}{\Delta t_{n-1}}(\tau-t_{n-1})+f(t_{n-1})\right]d\tau. \quad (A12)$$

Expending expression and adopting integration by parts, we can get

$$\int_{t_{n-1}}^{t_n} e^{-s_i(t_{n+1}-\tau)}\left[\frac{f(t_n)-f(t_{n-1})}{\Delta t_{n-1}}(\tau-t_{n-1})+f(t_{n-1})\right]d\tau$$

$$=\frac{f(t_n)-f(t_{n-1})}{\Delta t_{n-1}}\int_{t_{n-1}}^{t_n}e^{-s_v(t_{n+1}-\tau)}(\tau-t_{n-1})d\tau+f(t_{n-1})\int_{t_{n-1}}^{t_n}e^{-s_v(t_{n+1}-\tau)}d\tau$$

$$=\frac{f(t_n)-f(t_{n-1})}{s_v\Delta t_{n-1}}\int_{t_{n-1}}^{t_n}(\tau-t_{n-1})de^{-s_v(t_{n+1}-\tau)}$$

$$+\frac{f(t_{n-1})}{s_v}\Big[e^{-s_v\Delta t_n}-e^{-s_v(\Delta t_n+\Delta t_{n-1})}\Big].$$

$$(A13)$$

For the first term of equation A13, integration by parts is adopted again:

$$\frac{f(t_n)-f(t_{n-1})}{s_v\Delta t_{n-1}}\int_{t_{n-1}}^{t_n}(\tau-t_{n-1})de^{-s_v(t_{n+1}-\tau)}$$

$$=\frac{f(t_n)-f(t_{n-1})}{s_v\Delta t_{n-1}}\left[e^{-s_v\Delta t_n}\Delta t_{n-1}-\int_{t_{n-1}}^{t_n}e^{-s_v(t_{n+1}-\tau)}d\tau\right]$$

$$=\frac{f(t_n)-f(t_{n-1})}{s_v\Delta t_{n-1}}\left[e^{-s_v\Delta t_n}\Delta t_{n-1}-\frac{1}{s_v}\Big(e^{-s_v\Delta t_n}-e^{-s_v(\Delta t_n+\Delta t_{n-1})}\Big)\right].$$

$$(A14)$$

Combining the equation A11-A14, we can obtain

$$\int_{t_{n-1}}^{t_n}e^{-s_v(t_{n+1}-m)}f(m)dm$$

$$=\frac{e^{-s_v\Delta t_n}}{s_v^2\Delta t_{n-1}}\left[\begin{array}{l}\Big(e^{-s_v\Delta t_{n-1}}-1+s_i\Delta t_{n-1}\Big)f(t_n)\\+\Big(1-e^{-s_v\Delta t_{n-1}}-s_v e^{-s_v\Delta t_{n-1}}\Delta t_{n-1}\Big)f(t_{n-1})\end{array}\right]. \quad (A15)$$

REFERENCES

[1] K. Yoshioka and M. S. Zhdanov, "Three-dimensional nonlinear regularized inversion of the induced polarization data based on the Cole–Cole model," *Physics of the Earth and Planetary Interiors*, vol. 150, no. 1–3, pp. 29–43, May 2005.

[2] A. Revil, N. Florsch, and C. Camerlynck, "Spectral induced polarization porosimetry," *Geophysical Journal International*, vol. 198, no. 2, pp. 1016–1033, Aug. 2014.

[3] M. Schmutz, A. Revil, P. Vaudelet, M. Batzle, P. F. Viñao, and D. D. Werkema, "Influence of oil saturation upon spectral induced polarization of oil-bearing sands: IP signature of oil in sand," *Geophysical Journal International*, vol. 183, no. 1, pp. 211–224, Oct. 2010.

[4] G. Okay, P. Cosenza, A. Ghorbani, C. Camerlynck, J. Cabrera, N. Florsch, and A. Revil, "Localization and characterization of cracks in clay-rocks using frequency and time-domain induced polarization: *Induced polarization signature of cracks*," *Geophysical Prospecting*, vol. 61, no. 1, pp. 134–152, Jan. 2013.

[5] L. D. Slater and D. R. Glaser, "Controls on induced polarization in sandy unconsolidated sediments and application to aquifer characterization," *Geophysics*, vol. 68, no. 5, pp. 1547–1558, Sep. 2003.

[6] B. R. Spies, "A field occurrence of sign reversals with the transient electromagnetic method," *Geophys Prospect*, vol. 28, no. 4, pp. 620–632, Aug. 1980.

[7] M. Commer, P. V. Petrov, and G. A. Newman, "FDTD modeling of induced polarization phenomena in transient electromagnetics," *Geophysical Journal International*, vol. 209, no. 1, pp. 387–405, Jan. 2017.

[8] H. Li, G. Xue, and Y. He, "Decoupling induced polarization effect from time domain electromagnetic data in a Bayesian framework," *Geophysics*, vol. 84, no. 6, pp. A59–A63, Nov. 2019.

[9] D. Grombacher, E. Auken, N. Foged, T. Bording, N. Foley, P. T. Doran, J. Mikucki, H. A. Dugan, et al., "Induced polarization effects in airborne transient electromagnetic data collected in the McMurdo Dry Valleys, Antarctica," *Geophysical Journal International*, vol. 226, no. 3, pp. 1574–1583, May 2021.

[10] M. Commer, G. A. Newman, K. H. Williams, and S. S. Hubbard, "3D induced-polarization data inversion for complex resistivity," *Geophysics*, vol. 76, no. 3, pp. F157–F171, May 2011.

[11] J. H. Schon, *Physical Properties of Rocks A Workbook*. Elsevier, 2011.

[12] C. A. Dias, "Analytical model for a polarizable medium at radio and lower frequencies," *Journal of Geophysical Research*, vol. 77, no. 26, pp. 4945–4956, Sep. 1972.

[13] M. S. Zhdanov, "Generalized effective medium theory of induced polarization," *Geophysics*, vol. 37, no. 5, p. 11, Sep. 2008.

[14] K. S. Cole and R. H. Cole, "Dispersion and absorption in dielectrics I. alternating current characteristics," *The Journal of Chemical Physics*, vol. 9, no. 4, pp. 341–351, Apr. 1941.

[15] W. H. Pelton, S. H. Ward, P. G. Hallof, W. R. Sill, and P. H. Nelson, "Mineral discrimination and removal of inductive coupling with multifrequency IP," *Geophysics*, vol. 43, no. 3, pp. 588–609, Apr. 1978.

[16] H. O. Seigel, "Mathematical formulation and type curves for induced polarization," *Geophysics*, vol. 24, no. 3, pp. 547–565, Jul. 1959.

[17] P. and H. Debye, "The theory of electrolytes. I. Lowering of freezing point and related phenomena," *Physikalische Zeitschrift*, vol. 24, pp. 15–2066, Sep. 1923.

[18] B. K. Bhattacharyya, "Electromagnetic fields of a small loop antenna on the surface of a polarizable medium," *Geophysics*, vol. 29, no. 5, pp. 814–831, Oct. 1964.

[19] D. Guptasarma, "Computation of the time-domain response of a polarizable ground," *Geophysics*, vol. 47, no. 11, pp. 1574–1576, Nov. 1982.

[20] T. Lee, "The Cole-Cole model in time domain induced polarization," *Geophysics*, vol. 46, no. 6, pp. 932–933, Jun. 1981.

[21] D. Marchant, E. Haber, and D. W. Oldenburg, "Three-dimensional modeling of IP effects in time-domain electromagnetic data," *Geophysics*, vol. 79, no. 6, pp. E303–E314, Nov. 2014.

[22] X. Zhang, C. Yin, L. Wang, Y. Su, and Y. Liu, "3-D time-domain airborne EM forward modeling with IP effect based on implicit difference discretization of Caputo operator," *IEEE Transactions on Geoscience and Remote Sensing*, vol. 60, p. 5924110, Nov. 2022.

[23] A. Tarasov and K. Titov, "Relaxation time distribution from time domain induced polarization measurements," *Geophysical Journal International*, vol. 170, no. 1, pp. 31–43, Jul. 2007.

[24] P. R. Graves-Morris, G. A. Baker, and C. F. Woodcock, "Cayley's theorem and its application in the theory of vector Padé approximants," *Journal of Computational and Applied Mathematics*, vol. 66, no. 1, pp. 255–265, Jan. 1996.

[25] I. T. Rekanos and T. G. Papadopoulos, "An auxiliary differential equation method for FDTD modeling of wave propagation in Cole-Cole dispersive media," *IEEE Transactions on Antennas and Propagation*, vol. 58, no. 11, pp. 3666–3674, Nov. 2010.

[26] D. Marchant, "Induced polarization effects in inductive source electromagnetic data," Ph.d. thesis, University of British Columbia, 2015.

[27] H. Cai, X. Hu, B. Xiong, and M. S. Zhdanov, "Finite-element time-domain modeling of electromagnetic data in general dispersive medium using adaptive Padé series," *Computers & Geosciences*, vol. 109, pp. 194–205, Dec. 2017.

[28] Y. Ji, Y. Wu, S. Guan, and X. Zhao, "3D numerical modeling of induced-polarization electromagnetic response based on the finite-difference time-domain method," *Geophysics*, vol. 83, no. 6, pp. E385–E398, Nov. 2018.

[29] M. Zaslavsky, V. Druskin, and L. Knizhnerman, "Solution of 3D time-domain electromagnetic problems using optimal subspace projection," *Geophysics*, vol. 76, no. 6, pp. F339–F351, Nov. 2011.

[30] M. Zaslavsky and V. Druskin, "Solution of time-convolutionary Maxwell's equations using parameter-dependent Krylov subspace reduction," *Journal of Computational Physics*, vol. 229, no. 12, pp. 4831–4839, Jun. 2010.

[31] Y. Liu, L. Wang, C. Yin, X. Ren, B. Zhang, Y. Su, Z. Rong, and X. Ma, "3-D forward modeling of transient EM field in rough media using implicit time-domain finite-element method," *IEEE Transactions on Geoscience and Remote Sensing*, vol. 61, pp. 1–11, 2023.

[32] S. Jiang, J. Zhang, Q. Zhang, and Z. Zhang, "Fast evaluation of the Caputo fractional derivative and its applications to fractional diffusion equations," *Communications in Computational Physics*, vol. 21, no. 3, pp. 650–678, Mar. 2017.

[33] H. Sun and W. Cao, "A fast temporal second-order difference scheme for the time-fractional subdiffusion equation," *Numerical Methods Partial*, vol. 37, no. 3, pp. 1825–1846, May 2021.

[34] X. Bai and H. Rui, "An efficient FDTD algorithm for 2D/3D time fractional Maxwell's system," *Applied Mathematics Letters*, vol. 116, p. 106992, Jun. 2021.

[35] X. Bai, S. Wang, and H. Rui, "Numerical analysis of Finite-Difference Time-Domain method for 2D/3D Maxwell's equations in a Cole-Cole dispersive medium," *Computers & Mathematics with Applications*, vol. 93, pp. 230–252, Jul. 2021.

[36] F. Zheng, Z. Chen, and J. Zhang, "A finite-difference time-domain method without the courant stability conditions," *IEEE Microw. Guid. Wave Lett.*, vol. 9, no. 11, pp. 441–443, Nov. 1999.

[37] T. Namiki, "A new FDTD algorithm based on alternating-direction implicit method," *IEEE Trans. Microwave Theory Techn.*, vol. 47, no. 10, pp. 2003–2007, Oct. 1999.

[38] N. Feng, Y. Zhang, X. Tian, J. Zhu, W. T. Joines, and G. P. Wang, "System-combined ADI-FDTD method and its electromagnetic applications in microwave circuits and antennas," *IEEE Trans. Microwave Theory Techn.*, vol. 67, no. 8, pp. 3260–3270, Aug. 2019.

[39] J. C. Strikwerda, *Finite difference schemes and partial differential equations, second edition*. Society for Industrial and Applied Mathematics, 2004.

[40] N. Feng, Y. Zhang, and G. P. Wang, "Compact system-combined-based FDTD implementations with approximate Crank–Nicolson scheme and electromagnetic scattering," *IEEE Trans. Microwave Theory Techn.*, vol. 70, no. 2, pp. 1026–1036, Feb. 2022.

[41] G. Sun and C. W. Trueman, "Efficient implementations of the Crank-Nicolson scheme for the finite-difference time-domain method," *IEEE Trans. Microwave Theory Techn.*, vol. 54, no. 5, pp. 2275–2284, May 2006.

[42] S. Liu, C. Chen, and H. Sun, "Fast 3D transient electromagnetic forward modeling using BEDS-FDTD algorithm and GPU parallelization," *Geophysics*, vol. 87, no. 5, pp. E359–E375, Sep. 2022.

[43] A. Tarasov and K. Titov, "On the use of the Cole–Cole equations in spectral induced polarization," *Geophysical Journal International*, vol. 195, no. 1, pp. 352–356, Oct. 2013.

[44] K. Yee, "Numerical solution of initial boundary value problems involving maxwell's equations in isotropic media," *IEEE Transactions on Antennas and Propagation*, vol. 14, no. 3, pp. 302–307, May 1966.

[45] X. Ren, C. Yin, Y. Liu, J. Cai, C. Wang, and F. Ben, "Efficient modeling of time-domain AEM using finite-volume method," *Journal of Environmental & Engineering Geophysics*, vol. 22, no. 3, pp. 267–278, Sep. 2017.

[46] L. Thomas, *Elliptic Problems in Linear Difference Equations Over a Network*. Scientific Research, 1949.

[47] J. Wong, "An electrochemical model of the induced-polarization phenomenon in disseminated sulfide ores," *Geophysics*, vol. 44, no. 7, pp. 1245–1265, Jul. 1979.

[48] L. Han, Y. Ji, W. Ye, S. Wang, J. Lin, and X. Huang, "Seismoelectric wave propagation simulation by combining poro-viscoelastic anisotropic model with Cole–Cole depression model," *IEEE Transactions on Geoscience and Remote Sensing*, vol. 60, p. 510910, Jul. 2022.

[49] Y. Lin and C. Xu, "Finite difference/spectral approximations for the time-fractional diffusion equation," *Journal of Computational Physics*, vol. 225, no. 2, pp. 1533–1552, Aug. 2007.

[50] E. S. Um, J. M. Harris, and D. L. Alumbaugh, "An iterative finite element time-domain method for simulating three-dimensional electromagnetic diffusion in earth: Iterative finite element time-domain method," *Geophysical Journal International*, vol. 190, no. 2, pp. 871–886, Aug. 2012.

[51] D. W. Oldenburg, E. Haber, and R. Shekhtman, "Three dimensional inversion of multisource time domain electromagnetic data," *Geophysics*, vol. 78, no. 1, pp. E47–E57, Jan. 2013.

[52] M. Seidel and B. Tezkan, "1D Cole-Cole inversion of TEM transients influenced by induced polarization," *Journal of Applied Geophysics*, vol. 138, pp. 220–232, Mar. 2017.

[53] S. Li, H. Sun, X. Lu, and X. Li, "Three-dimensional modeling of transient electromagnetic responses of water-bearing structures in front of a tunnel face," *Journal of Environmental & Engineering Geophysics*, vol. 19, pp. 13–32, Mar. 2014.

[54] J. Chang, X. Wu, K. Lei, P. Lv, Y. Zhao, and Q. Meng, "Three-dimensional modeling of ground-airborne transient electromagnetic responses of typical models based on the finite difference approach," *Journal of Applied Geophysics*, vol. 197, p. 104545, Feb. 2022.

[55] W. Yu, R. Mittra, T. Su, Y. Liu, and X. Yang, *Parallel Finite-Difference Time-Domain Method*. Artech House, 2006.

[56] P. Weidelt, "Response characteristics of coincident loop transient electromagnetic systems," *Geophysics*, vol. 47, no. 9, pp. 1325–1330, Sep. 1982.

[57] L. Zhou, L. Yan, O. Kachaje, X. Xie, Y. Mao, and H. Zhang, "The simulation of transient electromagnetic based on time-domain IP model," *Journal of Environmental and Engineering Geophysics*, vol. 24, no. 1, pp. 159–162, Mar. 2019.

[58] R. S. Smith, P. W. Walker, B. D. Polzer, and G. F. West, "The time-domain electromagnetic response of polarizable bodies: an approximate convolution algorithm1," *Geophys Prospect*, vol. 36, no. 7, pp. 772–785, Oct. 1988.

Qi Zhao received his M.S. degree from the School of Resource and Civil Engineering, Northeastern University, Shenyang, China, in 2021. He is currently pursuing the Ph.D. degree from Geotechnical and Structural Engineering Research Center, Shandong University, Jinan, China. His main research interests include transient electromagnetic modeling and inversions with IP effects.

Huaifeng Sun received his Ph.D. degree from Geotechnical and Structural Engineering Research Center, Shandong University, Jinan, China, in 2013. He is currently a Professor at Shandong University and the head of Laboratory of Earth Electromagnetic Exploration, Shandong University. His research interests include modeling and inversion of geophysical electromagnetic data in engineering applications.

Shangbin Liu received his Ph.D. degree from Geotechnical and Structural Engineering Research Center, Shandong University, Jinan, China, in 2022. He is currently a Postdoctoral Research Fellow at Shandong University. His research focuses on the three-dimensional modeling and inversion of semi-airborne transient electromagnetic data.

Xushan Lu received his PhD degree from the Department of Earth Sciences, Memorial University of Newfoundland, St. John's, Canada, in 2020. He is currently a Research Associate at Memorial University of Newfoundland. His research focuses on the development of algorithms for modeling and inversion of geophysical electromagnetic data.

Xixian Bai received his Ph.D. degree from School of Mathematics, Shandong University, Jinan, China, in 2021. He is currently a lecturer with Zhengzhou University. His research interest includes the mathematical analysis of numerical algorithms for partial differential equations with special interests in finite-difference time-domain and finite element methods and their application to problems in physics and engineering.

Ziqiang Zheng received his B.S. and M.S. degree from Geotechnical and Structural Engineering Research Center, Shandong University, Jinan, China, in 2020 and 2023, respectively. He is currently a Research Associate at Geotechnical and Structural Engineering Research Center, Shandong University. His research focuses on data processing and algorithm development for transient electromagnetic data.